First-principles calculations of vacancies in semiconductors

First-principles Calculations of Vacancies in Semiconductors

半導体中原子空孔の第一原理計算

A dissertation submitted in partial fulfillment of the requirements for the degree "Doctor of Philosophy in Science"

Sholihun

1223102009

Supervisor : Prof. Mineo Saito

Graduate School of Natural Science and Technology

Division of Mathematical and Physical Sciences

Kanazawa University

July 2015

Dedicated to:
My father and mother for their endless love.
My beloved wife for her true love and spirit through all of my days.

List of publications:

1. **Sholihun**, Mineo Saito, Takahisa Ohno, and Takahiro Yamasaki, *Density-functional-theory-based calculations of formation energy and concentration of the silicon monovacancy*, Jpn. J. Appl. Phys., vol. **54**, pp. 041301, February 2015.

KANAZAWA UNIVERSITY

Abstract

Graduate School of Natural Science and Technology
Division of Mathematical and Physical Sciences

Doctor of Science

by Sholihun

The study of point defects in semiconductors has attracted much attention because of the crucial effects of such defects on various properties of materials. Some defects capture carriers and affect the electrical conductivity of semiconductors. Therefore, control of defects is necessary for device fabrication. Vacancies are fundamental defects, which are extensively studied theoretically and experimentally. We study the silicon vacancy by carrying out first-principles calculations based on quantum mechanics.

In this work, we use supercell model and consider the vibrational effect to calculate the vacancy concentration. We use large-scale supercells containing up to 1728-atomic sites for calculating the formation energy and up to 216-atomic sites for calculating the vibrational effect. We confirm the convergence of calculational results with respect to the cell size. The vibrational effect is computed from the phonon calculation by using harmonic approach. Without the vibrational effect, the concentration is much lower than the experimental estimates; thus, it is expected that the vibrational effect significantly contributes to the increase of the concentration.

Our results show that the formation energy is calculated to be 3.46 eV, and the vacancy concentration at the silicon melting point is estimated to be 7.4×10^{16} cm^{-3}. These values are consistent with experimental results. We find that the vibrational effect significantly increases the vacancy concentration about 10^4 times.

Acknowledgements

First of all, I would like to express my gratitude to Professor Mineo Saito. Thank you very much for your time, guidance and dedication during supervising me in completing this research and dissertation. I wish to express grateful acknowledgment to Professor Fumiyuki Ishii, Professor Tatsuki Oda, Professor Shinichi Miura, and Professor Hidemi Nagao for the discussion and comments. I also would like to thank the staffs of the Graduate School of Natural Science and Technology, Kanazawa University for their kind help and care during the years I was studying here.

I would like to thank the Directorate General of Higher Education (DIKTI), Indonesia, and Kanazawa University, Japan, for financial support through the Joint Scholarship Program.

I am thankful to all of computational science research group members. Thank you very much for all of your support and discussion. Indonesian friends, especially in Indonesian Student Association of Ishikawa (PPI Ishikawa) for their spirit.

Finally, deeply from my heart, I would like to thank my parents (Rasdi - Paringsih), my wife (Titan Parasita Siradj), and my children (Naila Atsmar Al Fikriyya and Najma Manar Alfadh) for their boundless love, understanding, endless patience and encouragement. I also would like to thank my two brothers (Riyanto - Sudiro) and my sister (Sugiharti) for their prayers, good wishes and support during my studies. The last but not least, I wish to express acknowledgment to my parents-in-law for the spirit and motivation.

Contents

List of Figures

List of Tables

Chapter 1

Introduction

1.1 Background

Semiconductor materials have been widely used in electronic devices such as transistor and light emitting diode. Computer, an electronic product that is necessary for our daily work, has a main part that is processor containing a large amount of semiconductor-based transistors. Thus, the quality of transistors plays an important role in enhancing the performance of the computer. In 1947, a germanium point-contact transistor was invented [1]. Several years later, a working silicon-based transistor was launched. At that time, silicon transistor replaced germanium transistor because of the ability of silicon to work in high-temperature operation in which germanium is restricted to low temperature.

Since the time of the invention of the silicon transistor, the development of silicon-based semiconductor devices has been so fast as the Moore's Law predicted [2]. Such devices are widely used in various electronic devices because of their capability to be downsized to several nanometers. One effort to enhance the performance of the semiconductor-based electronic devices is to understand their defect properties.

There are many types of defects (Fig. 1.1) such as vacancy, interstitial atom, and impurity atom. In this study, we are going to focus on vacancies in silicon and

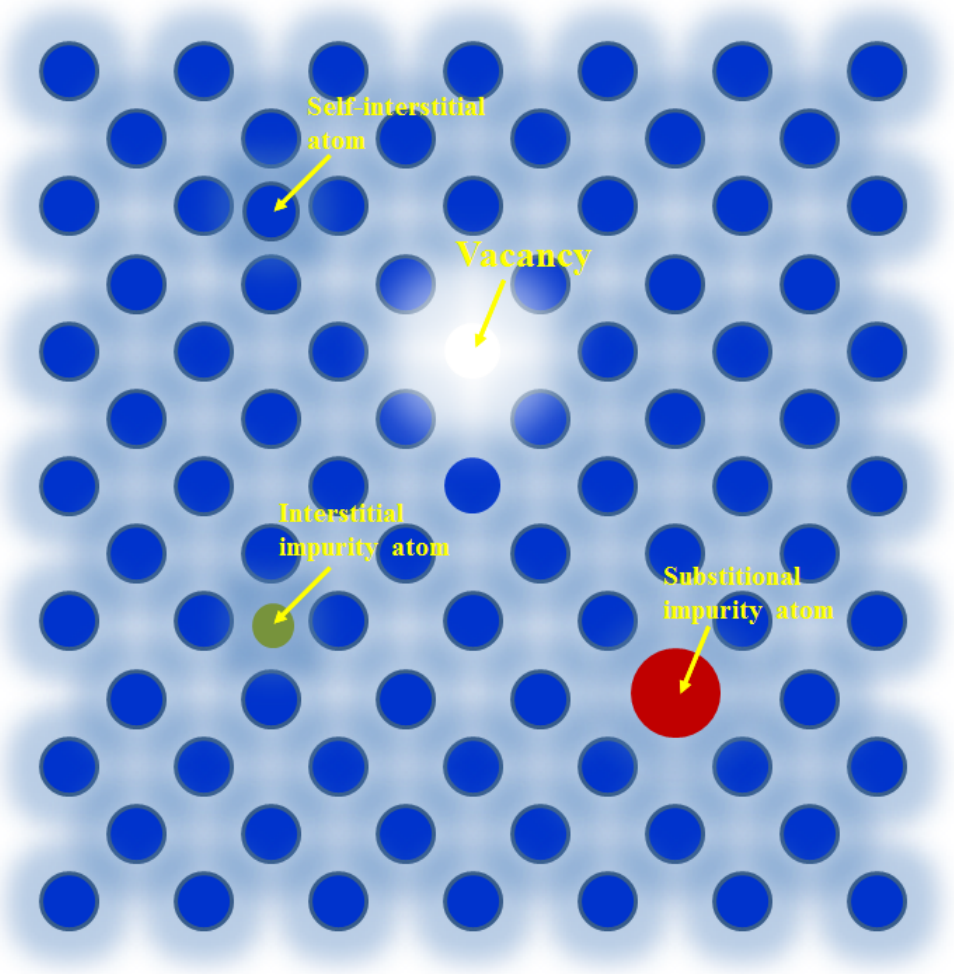

FIGURE 1.1: Some types of defects in semiconductor.

germanium. Vacancies in silicon have been investigated by studying their defects properties such as the formation energy and vacancy concentration.

The formation energy means energy required to form a certain configuration of defects. In other words, the formation energy may represent the stability of such defect configuration. Some previous studies investigated the defects properties; i.e., the formation energy of the silicon monovacancy. The formation energy of the silicon monovacancy was approximated to be 3.0 – 4.1 eV in the past theoretical [3–6] and experimental studies [7–11]. A converged value of the formation energy is necessary; i.e., to accurately calculate the concentration of the vacancy. An experimental result of the ultrasonic measurements [12] observed the monovacancy

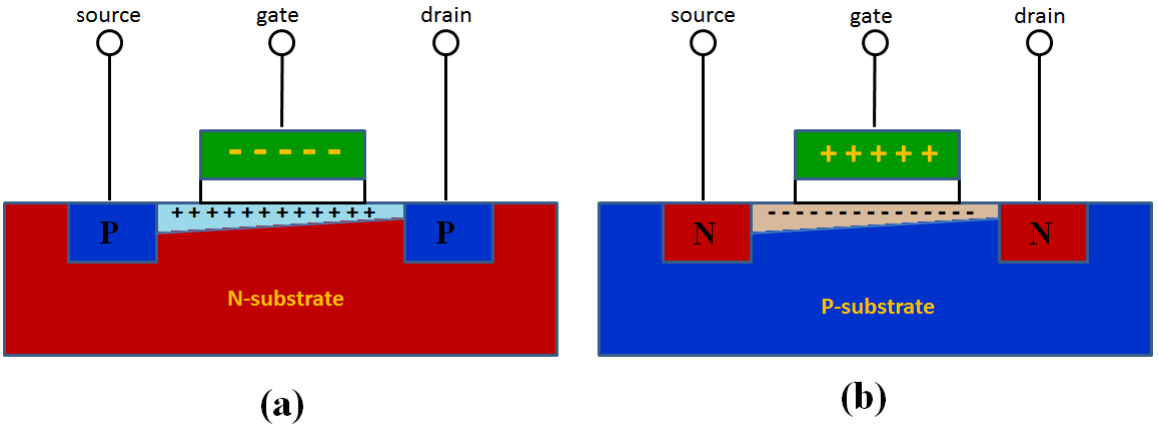

FIGURE 1.2: Schematic diagram of MOSFET: (a) PMOS and (b) NMOS.

and supposed that the concentration in low-temperature is found to be the same as that near the melting point. However, the defects observed by them might be different from the monovacancy as examined in previous studies [13, 14]. Therefore, the concentration of the silicon monovacancy near the melting point is a need to be clarified.

Recently, germanium is re-found to be a promising candidate as an active layer in electronic device; i.e, metal-oxide-semiconductor-field-effect-transistor (MOSFET) (Fig. 1.2) due to its high carrier mobility[15, 16]. As shown in Table 1.1, germanium has higher hole mobility than other semiconductor materials. In other word, germanium is suitable for P-type MOSFET (PMOS), whereas group III and V semiconductors are suitable for N-type MOSFET (NMOS). However, group III and V semiconductors such as gallium arsenide (GaAs) make mass production significantly more expensive than germanium; thus, germanium is still expected to be a promising candidate for NMOS [16]. Wu et al. [17] has recently carried out an experimental demonstration of complementary-metal-oxide-semiconductor (CMOS) circuits using germanium-based PMOS and NMOS. Their work supports the expectation that the use of germanium as a channel in CMOS enhances its performance.

It was reported that germanium is applicable for MOSFET that is possible to down-size to several nanometers; i.e., a 20-nm Ge-based CMOS inverters have been demonstrated by Wu et al. [17]. However, the performance of the Ge-based CMOS

TABLE 1.1: Carrier mobility of semiconductors [16, 18, 19].

Properties	Si	Ge	GaAs	InAs	InSb
Electron mobilty ($cm^2V^{-1}s^{-1}$)	1500	3900	9200	40000	77000
Hole mobility ($cm^2V^{-1}s^{-1}$)	450	1900	400	500	850

is needed to be enhanced [20–23]. An effort to enhance the performance of the semiconductor-based devices is to study the defect properties in the semiconductor materials. For this purpose, we study vacancies in germanium and present the discussion in Appendix.

In this study, we focus on the silicon monovacancy. We carry out a large-scale density-functional-theory calculation to accurately estimate the concentration of the silicon monovacancy. We use supercells containing 1728- and 216-sites for calculating formation energy and the vibrational effect on the concentration of the monovacancy, respectively.

1.2 Density Functional Theory as An Efficient Method

The development of information technology is supported by the invention of the electronic devices such as computer, mobile phone and television. Such devices contain materials whose characteristic determines the performance of the devices. Materials are characterized by the electronic structures, which are related to the electron behavior. Therefore, the understanding of the concept of electrons are necessary.

Electrons are considered as both particle and wave, called wave-particle duality. A usual way to describe the electron behavior is formulating it in the form of Schrödinger equation based on wavefunctions. We can find the electronic properties of such material from the wavefunctions, which are solved from the Schrödinger equation. However, a problem arises for a large and complex system containing

hundreds even thousands of atoms. For instance, a cluster consisting of 100 Pt atoms involves more than 23,000-dimensions wavefunctions [24]. This problem is difficult to be solved, even impossible for a more complex system. Therefore, an efficient method is needed to overcome this difficulty.

In 1998, Walter Kohn and John A. Popple were awarded the Nobel Prize in chemistry for their contribution in the practical and efficient method for solving the many-body problem, called the density functional theory (DFT). The key idea of DFT is to represent the many-body Schrödinger equation based on wavefunctions of an interacting system by single-particle Schrödinger equation based on electron density. Thus, we do not need to know the motion of every interacting particle in a system. We only need to know the density of valence electrons as a function of position. The DFT simplify the complex problem and reduce the dimensions from 3N variables to just three spatial variables of the electron density. By knowing only the electron density, we can calculate electronic properties of materials. The DFT as an efficient method can be computationally applied to solve a complex system consisting of thousands of atoms; thus, the DFT calculations are reliable in representing a real system.

1.3 The Purpose of Study

Vacancies in semiconductors are fundamental defects, which are extensively studied. We study the silicon monovacancy and calculate the concentration of the vacancy that is one of the important properties in controlling defects.

Clarification of the silicon monovacancy concentration at temperature near melting point is needed, because reliability of experiment of the concentration is not established. For this purpose, we carry out large-scale reliable calculations of the silicon monovacancy. We confirm the convergence of calculational results with respect to the cell size. In this calculation, we consider the vibrational effect, which is expected to significantly increase the concentration.

1.4 Outline of Dissertation

This dissertation consists of four chapters. In Chapter 1, the background of this research is introduced. We explain theory and application of the density functional theory in Chapter 2. In Chapter 3, we describe the calculational results of the vacancy concentration. In this chapter, we clarify the effect of the vibrational effect that significantly increases the concentration. The computational method used in the calculations is also given in this chapter. Finally, we give a summary and explain the future scope in Chapter 4.

We discuss symmetry and group theory, which are related to Chapter 3, in Appendix A. In Appendix B, we discuss the development of this study: stability of the multivacancies in germanium.

Chapter 2

Theory and Application of Density Functional Theory

The results in this dissertation are computed by using the first-principles density-functional-theory (DFT) calculations based on quantum mechanics. We use the PHASE [25] code to carry out the DFT calculations. The parameters used in the calculations are obtained from the optimization process. For instance, the lattice constant is obtained from the volume optimization with respect to total energies of the unit cell. The cutoff energy used for the volume optimization is obtained from checking convergence so that the formation energy difference between trial cutoff energies is not significant. We only use the atomic number and atomic positions, which are required in the first-principle calculations. Therefore, there is no empirical parameters employed in the DFT calculations. The use of the density functional reduces the dimension of the system; thus, the calculation of larger and more realistic systems is possible. The DFT calculations acquire a degree of accuracy, which provides comparable results with the experiments.

In this chapter, we explain a brief overview of the concept of the density functional theory. We explain the basis of the DFT in section 2.1. Next, we explain the application of the DFT in Section 2.2.

2.1 Basis of Density Functional Theory

A fully interacting Schrödinger equation of a complex system consisting of many electrons and nuclei is given by

$$\hat{H}\Psi(\mathbf{r_1}, \mathbf{R_1}, \mathbf{r_2}, \mathbf{R_2}, ...) = \mathbf{E}\Psi(\mathbf{r_1}, \mathbf{R_1}, \mathbf{r_2}, \mathbf{R_2}, ...) \tag{2.1}$$

where $\hat{H}$ is Hamiltonian operator and E is the eigen value representing a total energy of the system. $\mathbf{R_1}, \mathbf{R_2}, ...$ and $\mathbf{r_1}, \mathbf{r_2}, ...$ are the cartesian positions of the nuclei and the electrons, respectively. The Hamiltonian operator $\hat{H}$ is expressed as:

$$\hat{H} = \hat{T_e} + \hat{T_n} + \hat{V_{ee}} + \hat{V_{nn}} + \hat{V_{en}} \tag{2.2}$$

where $\hat{T_e}$ is the many-electrons kinetic energy operator , $\hat{T_n}$ is the many-nuclei kinetic energy operator, $\hat{V_{ee}}$ is the electron-electron interaction energy operator, $\hat{V_{nn}}$ is the nucleus-nucleus interaction energy operator, and $\hat{V_{en}}$ is the electron-nucleus interaction energy operator.

The kinetic energy operators are expressed as follows:

$$\begin{cases} \hat{T_e} = -\frac{1}{2}\sum_i^N \nabla_i^2(r_i), \\ \hat{T_n} = -\frac{1}{2}\sum_j \frac{1}{M_j}\nabla_i^2(R_j), \end{cases} \tag{2.3}$$

and the interaction energy operators are expressed as:

$$\begin{cases} \hat{V_{ee}} = \frac{1}{2}\sum_{i\neq j} \frac{1}{|\mathbf{r}_i - \mathbf{r}_j|} \\ \hat{V_{nn}} = \frac{1}{2}\sum_{i\neq j} \frac{Z_i Z_j}{|\mathbf{R}_i - \mathbf{R}_j|} \\ \hat{V_{en}} = -\sum_{i,j} \frac{Z_j}{|\mathbf{r}_i - \mathbf{R}_j|} \end{cases} \tag{2.4}$$

where the M_i, Z_i, and $\mathbf{R_i}$ are the mass of the i-th nucleus and the atomic number, respectively. This equation is too complex and difficult to be solved, even impossible for the system containing many complex atoms.

2.1.1 Born-Oppenheimer approximation

As mentioned above, the system represented by Eq. (2.2) is too complex and thus needs an approximation to simplify. Considering the large mass difference between a nucleus and an electron and assuming that the motion of the nuclei is negligible compared to that of the electrons, we neglect $\hat{T_n}$ and $\hat{V_{nn}}$. Therefore, the Hamiltonian operator in Eq. (2.2) is simplified as:

$$\hat{H} = \hat{T} + \hat{V_{ee}} + \hat{V_{en}}, \tag{2.5}$$

and the Schrödinger equation in Eq. (2.1) is then expressed as:

$$\hat{H}\Psi = \left[-\frac{1}{2}\sum_{i}^{N} \nabla^2 + \frac{1}{2}\sum_{i\neq j} \frac{1}{|\mathbf{r}_i - \mathbf{r}_j|} - \sum_{i,j} \frac{Z_j}{|\mathbf{r}_i - \mathbf{R}_j|} \right] \Psi = E\Psi, \tag{2.6}$$

This approximation method is called the *Born-Oppenheimer approximation*.

In the case of complex systems, although Eq. (2.6) is a simple form of Eq. (2.1), it needs a certain method to solve the eigenvalue problem. We next reduce our problem to a problem of finding the electronic ground state solutions. For this purpose, it is a need to introduce some approximations such as the variation principle and Hartree-Fock approximations. We first discuss the variation principle.

2.1.2 The variation principle

It is an impossible way to find any eigenfunction of the Hamiltonian operator, but we can consider all the many-body eigenfunctions ϕ_i. Assuming that the set of these eigenfunctions is complete, we can expand any other wavefunction ψ representing the same system as a linear combination of ϕ_i, given by

$$|\Psi\rangle = \sum_i c_i |\phi_i\rangle \tag{2.7}$$

where c_i are the expansion coefficients. The eigenstates $|\phi_i\rangle$ are assumed to be orthonormal, and the wavefunction is assumed to be normalized. Then the expectation value for the energy of the wavefunction is expressed as:

$$\begin{aligned} E &= \langle\Psi|\hat{H}|\Psi\rangle \\ &= \sum_{i,j} c_j^* c_i \langle\phi_i|\hat{H}|\phi_j\rangle \\ &= \sum_i |c_i^2| E_i \\ &\geq E_0 \sum_i |c_i^2| = E_0 \end{aligned} \tag{2.8}$$

where E_0 the ground state energy of $\hat{H}$, and $\sum_i |c_i^2| = 1$ because the wavefunction is normalized. The expectation value of the energy of any wavefunction ψ is thus higher than or equal to the ground state energy. In the computational point of view, this result is very important since this allows us to find the ground state energy and wavefunction by testing 'trial wavefunctions'. If the trial wavefunction is far from the true wavefunction, the calculation takes more computational cost, such as time consuming, even the calculation does not converge. Therefore, we need to find a trial wave function as close as the true wave function by employing certain technic.

We are going to present a technic for finding a good trial wavefunction. We assume that the approximate wavefunction can be expanded in terms of a set of plane waves, which is given by

$$\phi = \sum_j^N c_j \exp(-i\mathbf{k}\cdot\mathbf{r_j}). \tag{2.9}$$

Eq. (2.9) satisfies the minimum condition and is normalized, which is given by

$$\frac{\partial}{\partial c_j^*}\langle\phi|\hat{H}|\phi\rangle = 0 \tag{2.10}$$

for all c_j. We next introduce a parameter by introducing a new quantity which is given by

$$K = \langle\phi|\hat{H}|\phi\rangle - \lambda\left[\langle\phi|\phi\rangle - 1\right]. \tag{2.11}$$

Minimizing Eq. (2.11) with respect to c_j^* and λ, one obtains

$$\frac{\partial K}{\partial c_j^*} = \frac{\partial K}{\partial \lambda} = 0 \tag{2.12}$$

where λ is now called the *Lagrange multiplier*. Inserting Eq.(2.9) into Eq.(2.12), we get

$$\sum_j c_j \left(\langle exp(-i\mathbf{k}\cdot\mathbf{r_i})|\hat{H}|exp(-i\mathbf{k}\cdot\mathbf{r_j})\rangle = \lambda \langle exp(-i\mathbf{k}\cdot\mathbf{r_i})|exp(-i\mathbf{k}\cdot\mathbf{r_j})\rangle \right). \tag{2.13}$$

Then, a compact form of the eigenvalue equation is expressed as:

$$\sum_j H_{ij}c_j = \lambda \delta_{ij}. \tag{2.14}$$

Eq. (2.14) can be solved by calculating the matrix element H_{kj} and δ_{ij}. If Eq.(2.13) is multiplied by c_i^* and we sum it over i, an explicit form of is obtained, given by

$$\lambda = \frac{\sum_{i,j} c_i^* c_j \langle exp(-i\mathbf{k}\cdot\mathbf{r_i})|\hat{H}|exp(-i\mathbf{k}\cdot\mathbf{r_j})\rangle}{\sum_{i,j} c_i^* c_j \langle exp(-i\mathbf{k}\cdot\mathbf{r_i})|exp(-i\mathbf{k}\cdot\mathbf{r_j})\rangle}, \tag{2.15}$$

where λ corresponds to a different expectation value, and the eigenvector corresponds to the smallest eigenvalue resulting the best ϕ. The smallest eigenvalue is the closest approximation for the ground state energy. We next introduce an approximation method to simplify the problem, called the Hartree-Fock approximation.

2.1.3 The Hartree-Fock approximation

A main problem in solving the many-body Schrödinger equation is the representation of the many-body wavefunction. In 1920, D. Hartree [26] introduced an approach, named after himself, the Hartree approximation. The idea is to simplify the problem of electron-electron interactions by expanding the many-electron wavefunction into a product of single-electron wavefunction, which leads to solving the multi-electron Schrödinger equation of the wavefunction. Using this hypothesis

and employing the variation principle, we get N equations needed to be solved for an N single-electrons system. The wavefunction $\Psi(\mathbf{r_i})$ of this system is expressed as:

$$\Psi_H(\mathbf{r_1}, \mathbf{r_2}, \mathbf{r_3}, ...\mathbf{r_N}) = \frac{1}{\sqrt{N}}\phi(\mathbf{r_1}), \phi(\mathbf{r_2}), \phi(\mathbf{r_3}), ...\phi(\mathbf{r_N}) \tag{2.16}$$

where $\Psi(\mathbf{r_i})$ contains the spatial wavefunction $\phi(\mathbf{r_i})$.

However, the Hartree approximation does not consider the exchange interaction since Eq.(2.16) does not satisfy the Pauli's exclusion principle. The Hartree approximation is failed to cover the Pauli's exclusion principle since the Hartree product wavefunction is symmetric. Therefore, we need to introduce a reasonable approximation that has physical meaning. Then, Hartree and Fock introduced an approximation that deals with the concept that electrons are considered as distinguished particles. In the Hartree-Fock (HF) scheme, the system with N-electron wavefunction is approximated by an *antisymmetric* function.

The Hartree-Fock scheme is then described by using *Slater Determinant*, expressed as:

$$\Psi_{HF} = \frac{1}{\sqrt{N!}} \begin{vmatrix} \phi_1(\mathbf{r_1}) & \phi_2(\mathbf{r_1}) & \cdots & \phi_{N/2}(\mathbf{r_1}) \\ \phi_1(\mathbf{r_2}) & \phi_2(\mathbf{r_2}) & \cdots & \phi_{N/2}(\mathbf{r_2}) \\ \vdots & \vdots & \cdots & \vdots \\ \phi_1(\mathbf{r_N}) & \phi_2(\mathbf{r_N}) & \cdots & \phi_{N/2}(\mathbf{r_N}) \end{vmatrix}, \tag{2.17}$$

by introducing the additional orthonormal constraint:

$$\int \phi_i^*(\mathbf{r})\phi_i(\mathbf{r})d\mathbf{r} = \langle\phi_i|\phi_j\rangle = \delta_{ij}. \tag{2.18}$$

Using the above Slater Determinant, we can determine the HF energy from the expectation value of the Hamiltonian Eq.(2.6), given by

$$E = \langle\Psi_{HF}|\hat{H}|\Psi_{HF}\rangle = 2\sum_{i}^{N/2} h_i + \sum_{i}^{N/2}\sum_{j}^{N/2}(2J_{i,j} - K_{i,j}). \tag{2.19}$$

The first term of the Eq. (2.19) indicates the kinetic energy of electrons and interaction between electrons-nuclei. The second term represents the interaction between two electrons, called Coulomb and exchange integrals, where

$$h_i = \int \phi_i^*(\mathbf{r_1})\hat{h}\phi_i(\mathbf{r_1})d\mathbf{r_1} \tag{2.20}$$

$$\mathbf{J_{ij}} = \int\int \phi_i^*(\mathbf{r_1})\phi_i(\mathbf{r_1})\frac{1}{|\mathbf{r_1}-\mathbf{r_2}|}\phi_j^*(\mathbf{r_2})\phi_j(\mathbf{r_2})d\mathbf{r_1}d\mathbf{r_2} \tag{2.21}$$

$$\mathbf{K_{ij}} = \int\int \phi_i^*(\mathbf{r_1})\phi_j(\mathbf{r_1})\frac{1}{|\mathbf{r_1}-\mathbf{r_2}|}\phi_j^*(\mathbf{r_2})\phi_i(\mathbf{r_2})d\mathbf{r_1}d\mathbf{r_2} \tag{2.22}$$

The term $\mathbf{J_{ij}}$ is called the Coulomb integrals, which are found in the Hartree Approximation. Here, the exchange integral $\mathbf{K_{ij}}$ is introduced.

To present a simple way to understand the Coulomb and exchange interactions in Eq. (2.19), we consider V_{HF} as the Hartree-Fock potential. This potential describes the repulsive interaction between one electron and other N-1 electrons averagely, consisting Coulomb operator $\hat{J}$ and exchange operator $\hat{K}$, expressed as:

$$\hat{J}\phi(\mathbf{r}) = \int d\mathbf{r_2}\frac{|\text{Œ}_j(\mathbf{r_2})|^2}{|\mathbf{r_1}-\mathbf{r_2}|}\text{Œ}_i(\mathbf{r_1}) \tag{2.23}$$

$$\hat{K}\phi(\mathbf{r}) = \int d\mathbf{r_2}\frac{\text{Œ}_j^*(\mathbf{r_2})\,\text{Œ}_i(\mathbf{r_2})}{|\mathbf{r_1}-\mathbf{r_2}|}\text{Œ}_j(\mathbf{r_1}) \tag{2.24}$$

The Hartree-Fock scheme is constructed based on the effective wavefunction and potential. We guess the first set input of Slater determinant based on Pauli's principle and thus we have a reasonable approximation of the wavefunction. Then, we construct the potential operator by considering the electron's interaction, which is taken into account averagely, and considering the self-interaction in one electron. Next iteration is computed based on the new orbitals from the previous calculations until the convergence is reached. This technique is called as *self-consistent field* (SCF).

2.1.4 Density functional theory (DFT)

In Section 2.1, we discussed the Hartree-Fock approximation that deals with the exchange interaction. However, the Hartree-Fock equations neglect the correlation effect due to many-body interactions. Since the effects of electronic correlations are not negligible, a computationally efficient and practicable density-functional-theory scheme that covers both exchange and correlation effects are required. Nowadays, DFT is an efficient and practical method to describe ground state properties of materials due to high computational efficiency and good accuracy. The major idea of the DFT is to represent an interacting system by electron density, not wave functions. DFT is totally based on two theorems stated by Hohenberg and Kohn in 1964 [27]. In the following sections, we explain these two theorems.

2.1.4.1 Hohenberg-Kohn theorems

The work of Hohenberg and Kohn can be resumed as two important theorems. These theorems provide technics to determine the Hamiltonian operator and the properties of the system based on electron density. The electronic density $n(\mathbf{r})$ is given by

$$n(\mathbf{r}) = \mathbf{N} \sum_{\mathbf{s_1}} ... \sum_{\mathbf{s_N}} \int ... \int |\mathbf{\Psi}(\mathbf{r_1}, \mathbf{s_1}, \mathbf{r_2}, \mathbf{s_2}, ...\mathbf{r_N}, \mathbf{s_N})|^{\mathbf{2}} \mathbf{dr_1 dr_2}.....\mathbf{dr_N} \quad (2.25)$$

and

$$\int n(\mathbf{r}) d\mathbf{r} = N \quad (2.26)$$

Theorem I. (Hohenberg-Kohn 1) *In external potential of interacting particles for any system* $v_{ext}(\mathbf{r})$, *the potential* $v_{ext}(\mathbf{r})$ *is determined uniquely by the ground state particle density* $n_0(\mathbf{r})$.

Proof: The first theorem can be proved by *reductio ad absurdum*. Suppose that there were two different external potentials $v_{ext}^{(1)}(\mathbf{r})$ and $v_{ext}^{(2)}(\mathbf{r})$ which lead to the same ground state density $n(\mathbf{r})$. The two external potentials having two different Hamiltonian, $\widehat{H}^{(1)}$ and $\widehat{H}^{(2)}$, and different ground state wavefunction,$\psi^{(1)}$ and $\psi^{(2)}$,

are hypothesized to have the same ground state density $n_0(\mathbf{r})$. Since $\psi^{(2)}$ does not belong to the ground state of $\widehat{H}^{(1)}$, it follows that

$$E^{(1)} = \left\langle \psi^{(1)} \left| \widehat{H}^{(1)} \right| \psi^{(1)} \right\rangle < \left\langle \psi^{(2)} \left| \widehat{H}^{(1)} \right| \psi^{(2)} \right\rangle \tag{2.27}$$

The inequality of Eq.(2.27) is from the concept that the ground state is non-degenerate, which follows the arguments of Hohenberg and Kohn. The last term in Eq.(2.27) can be expressed as

$$\begin{aligned} \left\langle \psi^{(2)} \left| \widehat{H}^{(1)} \right| \psi^{(2)} \right\rangle &= \left\langle \psi^{(2)} \left| \widehat{H}^{(2)} \right| \psi^{(2)} \right\rangle + \left\langle \psi^{(2)} \left| \widehat{H}^{(1)} - \widehat{H}^{(2)} \right| \psi^{(2)} \right\rangle \\ &= E^{(2)} + \int d^3r \left[\upsilon_{ext}^{(1)}(\mathbf{r}) - \upsilon_{ext}^{(2)}(\mathbf{r}) \right] n_0(\mathbf{r}) \end{aligned} \tag{2.28}$$

then

$$E^{(1)} < E^{(2)} + \int d^3r \left[\upsilon_{ext}^{(1)}(\mathbf{r}) - \upsilon_{ext}^{(2)}(\mathbf{r}) \right] n_0(\mathbf{r}), \tag{2.29}$$

Using the same way, we can find the similar expression with Eq. (2.29) for $E^{(2)}$ just by exchanging superscripts (1) and (2),

$$E^{(2)} < E^{(1)} - \int d^3r \left[\upsilon_{ext}^{(1)}(\mathbf{r}) - \upsilon_{ext}^{(2)}(\mathbf{r}) \right] n_0(\mathbf{r}) \tag{2.30}$$

If we add Eq.(2.9) and Eq.(2.10), we arrive at the contradictory inequality $E^{(1)} + E^{(2)} < E^{(1)} + E^{(2)}$. This inequality means that there cannot be two different external potentials leading to the same non-degenerate ground-state charge density. Thus, the theorem is proved by *reductio ad absurdum.*

Theorem II. (Hohenberg-Kohn 2) *For any particular* $\upsilon_{ext}(\mathbf{r})$*, the exact ground state energy of the system is the global minimum value of this functional, and the density* $n(\mathbf{r})$ *that minimizes the functional is the exact ground state density* $n_0(\mathbf{r})$.

Proof: Since all properties such as the kinetic energy etc., are uniquely defined if $n(\mathbf{r})$ is specified, then each of such properties can be described as a functional of $n(\mathbf{r})$, along with the total energy functional

$$E_{HK}[n] = T[n] + E_{int}[n] + \int v_{ext}(\mathbf{r})\, n(\mathbf{r})\, d^3r + E_{II},$$

where E_{II} is the interaction energy of nuclei. Since the kinetic energy $T[n]$ and the internal potential energy $E_{int}[n]$ are the same for all systems, we describe them to be a universal functional $F[n]$; then, one gets

$$= F[n] + \int v_{ext}(\mathbf{r})\, n(\mathbf{r})\, d^3r + E_{II}. \tag{2.31}$$

We now consider a system with the ground state density $n^{(1)}(\mathbf{r})$ corresponding to external potential $v_{ext}^{(1)}(\mathbf{r})$, given by

$$\begin{aligned} E^{(1)} &= E_{HK}\left[n^{(1)}\right] \\ &= \left\langle \psi^{(1)} \left| \widehat{H}^{(1)} \right| \psi^{(1)} \right\rangle. \end{aligned} \tag{2.32}$$

Then, we introduce a different density, $n^{(2)}(\mathbf{r})$, corresponding to a different wavefunction $\psi^{(2)}$, given by

$$E^{(2)} = \left\langle \psi^{(2)} \left| \widehat{H}^{(1)} \right| \psi^{(2)} \right\rangle. \tag{2.33}$$

It follows immediately that the energy $E^{(2)}$ of this state is greater than $E^{(1)}$, since

$$\left\langle \psi^{(1)} \left| \widehat{H}^{(1)} \right| \psi^{(1)} \right\rangle < \left\langle \psi^{(2)} \left| \widehat{H}^{(1)} \right| \psi^{(2)} \right\rangle.$$

Minimizing $E^{(2)}$ with respect to $n(\mathbf{r})$ and expressing total energies of the system as a function of $n(\mathbf{r})$, one obtains the ground state energy. The correct density minimizing the energy is then addressed to the ground state density. In this way, DFT exactly reduces the N-body problem to the determination of a 3-dimensional

function $n(\mathbf{r})$ which minimizes the functional $E_{HK}[n(\mathbf{r})]$. However, the problem still remains that $E_{HK}[n(\mathbf{r})]$ is not known.

2.1.4.2 The Kohn-Sham equations

Kohn and Sham reformulated the problem in a more familiar form, leading to practical applications of DFT. They continued to prove the theorem stating that the total energy of the system depends only on the electron density of the system [28], expressed as:

$$E = E[n(\mathbf{r})]. \tag{2.34}$$

The idea is that an interacting electrons system is mapped into an auxiliary system of a non-interacting electrons with the same ground state charge density $n(r)$. For a system of non-interacting electrons, the ground-state charge density is represented as a sum over one-electron orbitals, given by

$$n(\mathbf{r}) = 2\sum_{i}^{N}|\Psi_i(\mathbf{r})|^2, \tag{2.35}$$

where i runs from 1 to $N/2$ if we consider the double occupancy of all states.

The electron density n($\mathbf{r}$) can be varied by changing the wave function $\Psi(\mathbf{r})$ of the system. If the electron density n($\mathbf{r}$) corresponds to the said wavefunction, then its total energy is the minimized energy, and the whole system is in a ground state. The Kohn-Sham approach is to replace an interacting-electrons system with a non-interacting-electrons system, which move in an effective potential [28]. The effective potential contains the external potential, Coulomb interaction between electrons, and the exchange and correlation interactions. By solving the equations, we can get the ground state density and energy. The accuracy of the solution is limited to the approximation of exchange and correlation interactions. It is convenient to write Kohn-Sham energy functional for the ground state including external potential as:

$$E_{KS} = T_s[n(\mathbf{r})] + E_H[n(\mathbf{r})] + E_{XC}[n(\mathbf{r})] + \int d\mathbf{r}V_{ext}(\mathbf{r})n(\mathbf{r}). \tag{2.36}$$

The first part of Eq. (2.36) is the kinetic energy of non-interacting electrons, expressed as:

$$T_s[n(\mathbf{r})] = -\frac{\hbar^2}{2m} 2 \sum_i \int \Psi_i^*(\mathbf{r}) \nabla^2 \Psi_i^*(\mathbf{r}) d\mathbf{r} \tag{2.37}$$

The second term is the Hartree energy containing the electrostatic interaction between cloud of charge:

$$E_H[n(\mathbf{r})] = \frac{e^2}{2} \int \frac{n(\mathbf{r}) n(\mathbf{r}')}{|\mathbf{r} - \mathbf{r}'|} d\mathbf{r} d\mathbf{r}' \tag{2.38}$$

All effects of exchange and correlation are grouped into exchange-correlation energy E_{XC}. If all the functional $E_{XC}[n(\mathbf{r})]$ were known, we could obtain exact ground state density and energy of the many-body problem.

Kohn-Sham energy problem is a minimization problem with respect to the density $n(\mathbf{r})$. Solution of this problem can be obtained by using functional derivative as follows :

$$\begin{aligned} \frac{\delta E_{KS}}{\delta \Psi_i^*(\mathbf{r})} &= \frac{\delta T[n]}{\delta \Psi_i^*(\mathbf{r})} + \left[\frac{\delta E_{ext}[n]}{\delta n(\mathbf{r})} + \frac{\delta E_H[n]}{\delta n(\mathbf{r})} + \frac{\delta E_{XC}[n]}{\delta n(\mathbf{r})} \right] \frac{\delta n(\mathbf{r})}{\delta \Psi_i^*(\mathbf{r})} \\ &\quad - \frac{\delta \left(\lambda \left(\int n(\mathbf{r}) d\mathbf{r} - N \right) \right)}{\delta n(\mathbf{r})} \left[\frac{\delta n(\mathbf{r})}{\delta \Psi_i^*(\mathbf{r})} \right] = 0, \end{aligned} \tag{2.39}$$

where λ is Lagrange multiplier and the exchange-correlation potential V_{XC} is given by the functional derivative

$$V_{XC} = \frac{\delta E_{XC}[n]}{\delta n(\mathbf{r})}. \tag{2.40}$$

Since

$$\frac{\delta n(\mathbf{r})}{\delta \Psi_i^*(\mathbf{r})} = \Psi_i(\mathbf{r}),$$

the last term is the Lagrange multiplier for handling the constraints so that we can get a non-trivial solution.

The first, second, and third terms of Eq. (2.39) are given by

$$\frac{\delta T[n]}{\delta \Psi_i^*(\mathbf{r})} = -\frac{\hbar^2}{2m} 2\nabla^2 \Psi_i(\mathbf{r}), \tag{2.41}$$

$$\left[\frac{\delta E_{ext}[n]}{\delta n(\mathbf{r})} + \frac{\delta E_H[n]}{\delta n(\mathbf{r})} + \frac{\delta E_{XC}[n]}{\delta n(\mathbf{r})}\right] \frac{\delta n(\mathbf{r})}{\delta \Psi_i^*(\mathbf{r})} = 2(V_{ext}(\mathbf{r}) + V_H(\mathbf{r}) + V_{XC}(\mathbf{r}))\Psi_i(\mathbf{r}),$$

$$\frac{\delta\left(\lambda\left(\int n(\mathbf{r})d\mathbf{r} - N\right)\right)}{\delta n(\mathbf{r})}\left[\frac{\delta n(\mathbf{r})}{\delta \Psi_i^*(\mathbf{r})}\right] = 2\varepsilon_i \Psi_i(\mathbf{r}) \tag{2.42}$$

Inserting Eq. (2.41) and (2.42) to Eq. (2.39), we can obtain Kohn-Sham equation satisfying many-body Schrödinger equation.

$$\left[-\frac{1}{2}\nabla^2 + V_{KS}(\mathbf{r})\right]\Psi_i(\mathbf{r}) = \varepsilon_i \Psi_i(\mathbf{r}) \tag{2.43}$$

where

$$V_{KS}(\mathbf{r}) = V_{ext}(\mathbf{r}) + V_H(\mathbf{r}) + V_{XC}(\mathbf{r}) \tag{2.44}$$

or,

$$V_{KS}(\mathbf{r}) = V_{ext}(\mathbf{r}) + \frac{e^2}{2}\int \frac{n(\mathbf{r}')}{|\mathbf{r} - \mathbf{r}'|} d\mathbf{r}' + V_{XC}(\mathbf{r}). \tag{2.45}$$

If the virtual independent-particle system has the same ground state as the real interacting system, then the many-electron problem reduces to one electron problem. Thus we can write:

$$V_{KS}(\mathbf{r}) = V_{eff}(\mathbf{r}) \tag{2.46}$$

The kinetic energy $T_s[n(\mathbf{r})]$ is given by

$$T_s[n(\mathbf{r})] = \sum_i \varepsilon_i - \int n(\mathbf{r}) V_{eff}(\mathbf{r}) d\mathbf{r} \tag{2.47}$$

Substituting this formula in Eq. (2.36), one obtains the total energy, given by

$$E_{KS}[n(\mathbf{r})] = \sum_i \varepsilon_i + \frac{1}{2}\int\int \frac{n(\mathbf{r})n(\mathbf{r}')}{|\mathbf{r} - \mathbf{r}'|} d\mathbf{r} d\mathbf{r}' + E_{xc}[n] - \int n(\mathbf{r}) V_{eff}(\mathbf{r})) d\mathbf{r} \tag{2.48}$$

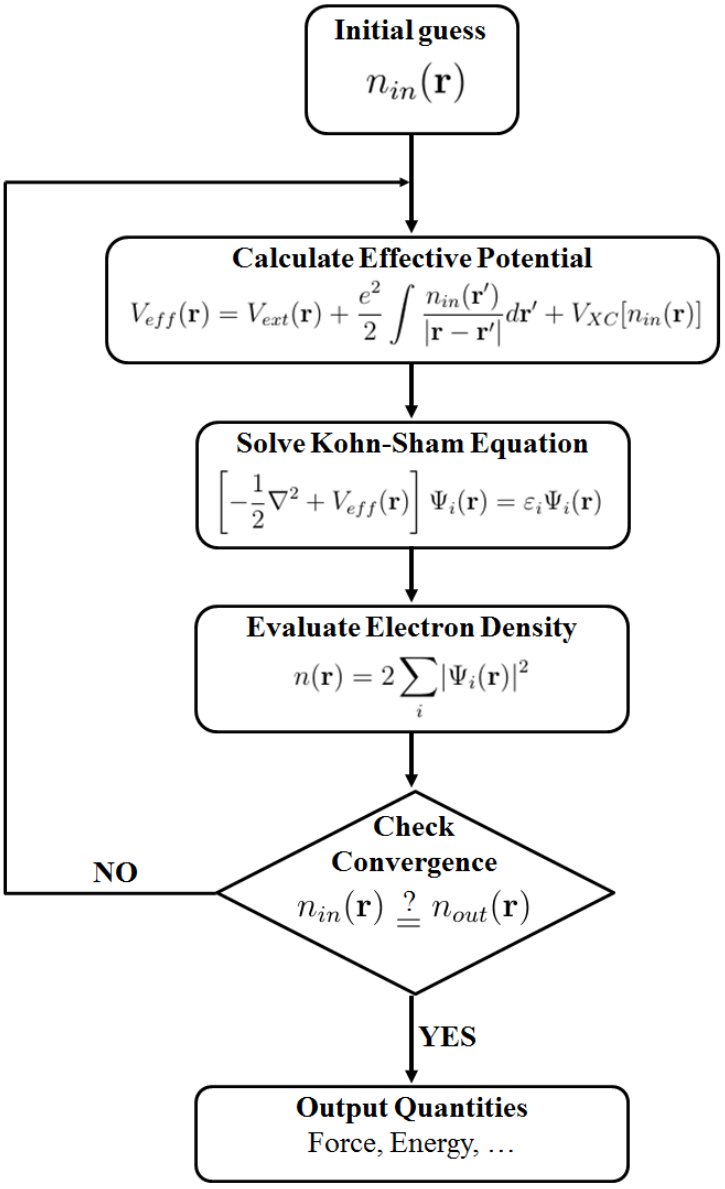

FIGURE 2.1: Self-consistent scheme of Kohn-Sham equation.

Since the Hartree term and V_{xc} depend on $n(\mathbf{r})$, which depend on Ψ_i, the Kohn-Sham equation should be solved in an iterative self-consistent way. Starting from an initial guess for $n(\mathbf{r})$ and then calculating the corresponding V_H and V_{xc}, the Kohn-Sham equations for the Ψ_i can be solved, producing a new density that will be used as a new initial guess in the next iterative step. This procedure is then repeated until the convergence is reached. This iterative procedure is described in a flowchart as shown in Fig. 2.1.

2.1.5 Exchange and correlation functional

As we know from the previous section that the major problem of DFT comes from the exact unknown-functionals for exchange and correlation, except for the free-electron gas. The many-body problems are re-written as the effective one-electron problem by using the Kohn-Sham equation. However, the Kohn-Sham equation cannot be solved since the derivative $E_{XC}[n(\mathbf{r})]$ is unknown. Therefore, it is a need to have an accurate exchange-correlation energy $E_{XC}[n(\mathbf{r})]$ or potential $V_{XC}(\mathbf{r})$ functional in order to give a satisfactory description of a realistic condensed-matter system. The familiar exchange-correlation functionals widely used are the local density approximation (LDA) and generalized gradient approximation (GGA) functionals that we are going to discuss in the section.

2.1.5.1 Local density approximation (LDA)

Since the functional $E_{XC}[n(\mathbf{r})]$ is unknown, one has to find a good approximation for it. A simple approximation based on homogeneous electron gas (HEG), which was suggested by Hohenberg and Kohn, is the LDA or in the spin polarized case the local-spin-density approximation (LSDA). The exchange-correlation energy per particle $e_{XC}[n(\mathbf{r})]$ is expressed as:

$$\begin{aligned} E_{xc}^{LDA}[n(\mathbf{r})] &= \int n(\mathbf{r}) e_{xc}^{homo}(n(\mathbf{r}))d\mathbf{r} \\ &= \int n(\mathbf{r}) \left[e_x^{homo}(n(\mathbf{r})) + e_c^{homo}(n(\mathbf{r}))\right] d\mathbf{r}, \end{aligned} \tag{2.49}$$

and for the spin polarized system, given by

$$E_{xc}^{LSDA}[n_+(\mathbf{r}), n_-(\mathbf{r})] = \int n(\mathbf{r}) e_{xc}^{homo}(n_+(\mathbf{r}), (n_-(\mathbf{r}))d\mathbf{r}. \tag{2.50}$$

The exchange energy $e_x(n(\mathbf{r}))$ is given by

$$e_x^{LDA}(n(\mathbf{r})) = -\frac{3}{4\pi} k_f, \tag{2.51}$$

where the Fermi wavevector $k_f = (3\pi^2 n)^{\frac{1}{3}}$.

The expression of the correlation energy density of the HEG at high-density limit is defined as:

$$e_c = Aln(r_s) + B + r_s(Cln(r_s) + D), \tag{2.52}$$

and the density limit has the form

$$e_c = \frac{1}{2}\left(\frac{g_0}{r_s} + \frac{g_1}{r_s^{3/2}} + ...\right), \tag{2.53}$$

where the Wigner-Seitz radius r_s is related to the density as:

$$r_s = (3/(4\pi n))$$

13. (2.54)

As for spin-polarized systems, the exchange energy functional is known exactly from the result of spin-unpolarized functional:

$$E_x[n_+(\mathbf{r}), n_-(\mathbf{r})] = \frac{1}{2}(E_x[2n_+(\mathbf{r})] + E_x[2n_-(\mathbf{r})]). \tag{2.55}$$

The spin correlation energy density $e_c(n(\mathbf{r}),\ \xi(\mathbf{r})$ is constructed to interpolate extreme values $\xi = 0, \pm 1$, corresponding to spin-unpolarized and ferromagnetic situations. The exchange-correlatiomn potential $V_{XC}(n(\mathbf{r}))$ in LDA is given by

$$\frac{\delta E_{XC}[n]}{\delta n(\mathbf{r})} = \int d\mathbf{r}\left[\epsilon_{xc} + n\frac{\partial \epsilon_{xc}}{\partial n}\right] \tag{2.56}$$

$$V_{XC}(\mathbf{r}) = \epsilon_{xc} + n\frac{\partial \epsilon_{xc}}{\partial n}, \tag{2.57}$$

$$E_{XC}[n] = \int d\mathbf{r} n(\mathbf{r})\epsilon_{xc}([n], \mathbf{r}), \tag{2.58}$$

where $\epsilon_{xc}([n], \mathbf{r})$ is the energy per electron that depends only on the density $n(\mathbf{r})$.

2.1.5.2 Generalized gradient approximation (GGA)

As explained above that the LDA is used as an approach to the homogeneous electron gas. In the case of the inhomogeneous density, we have to introduce the expansion of electronic density in the term of gradient and higher order derivatives, which are usually called as the generalized gradient approximation (GGA). The GGA is still local but also take into account the gradient of the density at the same coordinate. Three most widely used GGAs are those proposed by Becke [29] (B88) , Perdew et al. [30, 31], and Perdew, Burke and Enzerhof [32] (PBE). The exchange-correlation energy functional of the GGA is the generalized form of Eq. (2.50) which includes corrections from density gradient $\nabla n(\mathbf{r})$, defined as:

$$E_{xc}^{GGA}[n_+(\mathbf{r}), n_-(\mathbf{r})] = \int n(\mathbf{r}) e_{xc}[n(\mathbf{r}) F_{XC}[n(\mathbf{r}), |\nabla n_+(\mathbf{r})|, |\nabla n_-(\mathbf{r})|, ...] d\mathbf{r} \tag{2.59}$$

F_{XC} is the escalation factor that modifies the LDA expression due to the variation of the density around the considered point [33]. The exchange energy expansion will introduce a term that proportional to the squared gradient of the density. If we consider up to fourth order, the similar term also appears commensurate with the square of the density's Laplacian. Recently, the general derivation of the exchange-gradient expansion has been up to sixth order by using second-order density-response-theory [34]. The lowest order (fourth order) terms in the expansion of F_x have been calculated analytically [34, 35], which is given by

$$F_X(m, n) = 1 + \frac{10}{81} m + \frac{146}{2025} m^2 - \frac{73}{405} nm + Dm^2 + O(\nabla\rho^6) \tag{2.60}$$

where

$$m = \frac{|\nabla\rho|^2}{4(3\pi^2)^{2/3}\rho^{8/3}}, \tag{2.61}$$

and

$$n = \frac{\nabla^2\rho}{4(3\pi^2)^{2/3}\rho^{5/3}} \tag{2.62}$$

are the reduced density gradient and reduced Laplacian of density, respectively.

There are some descriptions of GGA compared with LDA (LSDA):

1. GGA enhances the binding energies and atomic energies,
2. GGA enhances the energetics, geometries, and dynamical properties of water, ice, and water clusters,
3. Semiconductors are marginally better described within the LDA than in GGA, except for binding energies,
4. For *4d-5d* transition metals, the improvement of GGA over LDA is not clear, depends on how well the LDA does in each particular case,
5. Lattice constant of noble metals (Ag, Au, and Pt) are overestimated in GGA.

2.1.6 Plane waves method

We are now able to solve the Kohn-Sham equation (Eq. (2.43)) since the exchange-correlation functionals were introduced. The next step is to reach the equilibrium geometries by evaluating the atomic forces. For this purpose, the plane-wave method is employed. Plane waves are not centered at the nuclei but extend throughout the complete space. They implicitly involve the concept of periodic boundary condition. In practice, the Kohn-Sham equation is described by using the plane waves. The periodic arrangement of the atoms within the cell in the real space requires the wave functions satisfying Bloch's theorem, which can be expressed as:

$$\Psi_i(\mathbf{r}) = \exp(\mathbf{ik} \cdot \mathbf{r})\mathbf{u_k}(\mathbf{r}), \tag{2.63}$$

where $u_k(\mathbf{r})$ is periodic in space, which can be expanded into a set of plane waves

$$u_i(\mathbf{r}) = \sum_{\mathbf{G}} c_{i,\mathbf{G}} exp(i\mathbf{G} \cdot \mathbf{r}) \tag{2.64}$$

Inserting Eq. (2.64) to Eq. (2.63), each electronic wave function can be expressed as:

$$\Psi_i(\mathbf{r}) = \sum_{\mathbf{G}} c_{i,\mathbf{k+G}} exp(i(\mathbf{k} + \mathbf{G}) \cdot \mathbf{r}) \tag{2.65}$$

Kohn-Sham equation (Eq. (2.43)) is then substituted in terms of reciprocal space **k** as follows:

$$\sum_{\mathbf{G'}} \left[\frac{1}{2} |\mathbf{k+G}|^2 \delta_{G,G'} + V_{KS}(\mathbf{G\text{-}G'}) \right] c_{i,\mathbf{k+G}} = \varepsilon_i c_{i,\mathbf{k+G}} \tag{2.66}$$

The solution of the Kohn-Sham equation is obtained by diagonalizing the Hamiltonian matrix. The diagonal part represents the kinetic term, otherwise represent the potential term. To limit the summation over **G**, cutoff energy is applied to the kinetic term, which is expressed as:

$$E_{cut} = \frac{1}{2} |\mathbf{k+G}|^2 \equiv \mathbf{G}_{cut}^2 \tag{2.67}$$

The limitation of the cutoff energy is necessary by setting a computationally-reasonable cutoff energy value.

2.1.7 Pseudopotential

Maximum number of plane waves is required to expand the tightly-bonded core electrons; thus the large value of cutoff energy is needed. However, the large cutoff energy means increasing the computational cost even making the calculation unreasonable; i.e., consuming more time. Therefore, it is necessary to introduce an approach to replace the effects of the tightly-bound core electrons. Another effect we should consider is the strong Coulomb potential of the nuclei. Since valence electrons affect more significantly than the core electrons of the electron structure, an effective ionic potential acting on the valence electrons, called pseudopotential, can be introduced. The usage of the pseudopotential is to replace the Coulomb potential of the nuclei and the effects of the tightly-bound core electrons. There are two types of famous pseudopotentials, the norm-conserving and ultrasoft pseudopotentials.

2.1.7.1 Norm-conserving pseudopotential

This type of pseudopotential should follow some requirements [36] which are:

1. All the electrons and pseudo valence eigenvalues are the same as the selected atomic configuration,

$$\epsilon_i^{AE} = \epsilon_i^{PS}. \tag{2.68}$$

2. All the electrons and pseudo valence eigenvalues are in agreement in an external core region,

$$\Psi_i^{AE}(r) = \Psi_i^{PS}(r), \quad r \geq R_c. \tag{2.69}$$

3. The logarithmic derivatives and their first energy derivative of real and pseudo wavefunctions match at the cutoff radius R_c,

$$\frac{d}{dr} \ln \Psi_i^{AE}(r) = \frac{d}{dr} \ln \Psi_i^{PS}(r). \tag{2.70}$$

4. The total charge inside core radius R_c for each wave function must be same (norm conservation),

$$\int_0^{R_c} dr |\Psi_i^{AE}(r)|^2 = \int_0^{R_c} dr |\Psi_i^{PS}(r)|^2. \tag{2.71}$$

5. The logarithmic derivatives of all-electron and pseudo wavefunctions must be same for $r \geq R_c$. This condition is implied by point 4.

2.1.7.2 Ultrasoft pseudopotential

The ultrasoft pseudopotential is introduced to obtain smoother pseudo-wavefunctions [37]. The pseudo-wavefunctions are classified into two parts:

1. Ultrasoft valence wavefunctions that omit norm conservation criteria ϕ_i^{US}.

2. A core augmentation charge.

$$Q_{nm}(r) = \Psi_n^{AE*}(r)\Psi_m^{AE}(r) - \Psi_n^{US*}(r)\Psi_m^{US}(r) \tag{2.72}$$

The ultrasoft pseudopotential takes the form of

$$V^{US} = V_{loc}(r) - \sum_{nmI} D_{nm}^0 |\beta_n^I\rangle\langle\beta_m^I|, \tag{2.73}$$

where β is projector function, which is expressed as:

$$|\beta_n\rangle = \sum_m \frac{|X_m\rangle}{\langle X_m|\phi_n\rangle}, \tag{2.74}$$

and they are strictly localized inside the cutoff region for the wavefunctions, and the X - functions are defined as:

$$|X_n\rangle = (\epsilon_n - \hat{T} - V_{loc})|\phi_n\rangle \tag{2.75}$$

$$D_{nm}^0 = \langle\phi_n|X_m\rangle + \epsilon_m q_{nm}. \tag{2.76}$$

The scattering properties of the pseudopotential can be improved by using more than one β projector function per angular momentum channel.

It is necessary to use the generalized eigenvalue formalism. For this purpose, we introduce the overlap operator S

$$\hat{S} = \mathbf{1} + \sum_{nmI} q_{nm}|\beta_n^I\rangle\langle\beta_m^I|, \tag{2.77}$$

where

$$q_{nm} = \int_0^{r_c} dr Q_{nm}(r) \tag{2.78}$$

Finally, the charge density is defined as:

$$n(\mathbf{r}) = \sum_i \phi_i^*(r)\hat{S}\phi_i(r) \tag{2.79}$$
$$= \sum_i \left[|\phi_i(\mathbf{r})|^2 + \sum_{nmI} Q_{nm}^I(\mathbf{r}) \langle \phi_i | \beta_n^I \rangle \langle \beta_m^I | \phi_i \rangle \right].$$

2.2 Application of the Density Functional Theory

In the previous section, we explained the basis of the density functional theory (DFT). We are going to present applications of the DFT in the crystal system. The DFT can be employed to calculate the lattice constant, phonon calculation, density of states and so on. We first explain the optimization process of the lattice constant.

2.2.1 Lattice constant optimization

An important process required in the DFT calculations is lattice constant optimization; thus, this process is conducted in the calculations, which are going to be discussed in Chapter 3. We carry out the DFT calculations based on the generalized gradient approximation (GGA). We use the norm-conserving pseudopotential and 9 Ryd cutoff energy for the plane wave basis set.

We calculate the lattice constant by optimizing the cell volume over the total energy. We use the Birch-Murnaghan equation of states (BM-EOS) to accurately compute the optimized lattice constant. The BM-EOS is given by [38, 39]

$$E(V) = E_0 + \frac{9}{16} V_0 B_0 [(Z-1)^3 B_0' + (Z-1)^2(6-4Z)], \tag{2.80}$$

where $Z = \left(\frac{V_0}{V}\right)^{2/3}$. E_0, V_0, B_0, and B_0' are determined from the curve-fitting, which are the minimum energy, cell volume at E_0, bulk modulus at V_0, and first-derivative of the bulk modulus at $V = V_0$, respectively.

The BM-EOS is computed using the least-square minimization. The optimization process is conducted numerically by using Levenberg-Marquardt method (LM) [40, 41]. The LM method combines Gauss-Newton and steepest-descent methods to decrease the iteration steps so that the convergence can be reached rapidly. Let the model curve is given by

$$E(V) = E(y) = f(x_i, \alpha_j), \quad i = 1, 2, ..., n \quad j = 1, 2, ..., m \tag{2.81}$$

where $E(y)$ is the estimated value of y, and x_i is the independent variable. $f(x_i, \alpha_j)$ is fitted to the datum pairs (x_i, y_i).

The parameter α is then optimized by minimizing

$$\xi(\alpha_j) = \sum_i^n [y_i - f(x_i, \alpha_j)]^2. \tag{2.82}$$

In each step of iteration, α is updated by a correction δ to be $(\alpha + \delta)$. Expanding $f(x_i, \alpha_j)$ in Taylor series gives

$$\begin{aligned} f(x_i, \alpha_j + \delta_j) &= f(x_i, \alpha_j) + \sum_j^m \left(\frac{\partial f_i}{\partial \alpha_j} \right) \delta_j \\ &= f(x_i, \alpha_j) + J_i \delta_j, \end{aligned} \tag{2.83}$$

where J_i is gradient of f_i. Substituting Eq. 2.83 to Eq. 2.82 gives

$$\begin{aligned} \xi(\alpha_j + \delta_j) &= \sum_i^n [y_i - f(x_i, \alpha_j) - J_i \delta_j]^2 \\ &= \left\| \mathbf{y} - \mathbf{f}(\boldsymbol{\alpha}) - \mathbf{J}\boldsymbol{\delta} \right\|^2, \end{aligned} \tag{2.84}$$

Minimizing ξ by taking the first derivative over δ follows

$$\frac{\partial \xi(\alpha_j + \delta_j)}{\partial \delta_j} = 0 \tag{2.85}$$

$$\mathbf{J}^T[\mathbf{y} - \mathbf{f}(\boldsymbol{\alpha})] - \mathbf{J}^T\mathbf{J}\boldsymbol{\delta} = 0$$

$$(\mathbf{J}^T\mathbf{J})\boldsymbol{\delta} = \mathbf{J}^T[\mathbf{y} - \mathbf{f}(\boldsymbol{\alpha})], \tag{2.86}$$

Then, by introducing the damping factor λ, the LM algorithm is given by

$$[\mathbf{J}^T\mathbf{J} + \lambda \mathbf{diag}(\mathbf{J}^T\mathbf{J})]\boldsymbol{\delta} = \mathbf{J}^T[\mathbf{y} - \mathbf{f}(\boldsymbol{\alpha})], \tag{2.87}$$

where $\mathbf{J}$ is Jacobian matrix. $\mathbf{f}$ and $\mathbf{y}$ are two vectors containing parameters of $f(x_i, \alpha_j)$ and y_i, respectively.

The calculation of the BEM-EOS requires guess parameters. If the guess parameters are closer to the exact values, the iteration reaches the convergence faster. Farther from the exact values, the iteration steps increase, even the calculation does not reach the convergence. To overcome this problem, we use guess parameters obtained from the second-order polynomial fitting. The second-order polynomial fit doest not acquire accurate extracted-parameters. However, the use of the polynomial fitting reduces the iteration steps; thus, the convergence is reached rapidly.

The calculated results of the BM-EOS fitting are given in Figs. (2.2) and (2.3) for silicon and germanium, respectively. The BM-EOS gives accurate results, which are shown by a good fit between the input data (closed-circles) and the curve model (solid line). The optimized lattice constants are 5.604 Å for germanium and 5.466 Å for silicon, which are close to the experimental values of 5.657 Å (Ge) [42] and 5.431 Å (Si) [43]. Therefore, our calculations well reproduce the experimental results. The optimized lattice constant is then used in the DFT calculations in all supercell systems.

2.2.2 Vibrational frequency

The optimized lattice constant is then used to calculate the defect properties of materials such as vibrational frequencies. The vibrational frequencies are needed to calculate the vacancy concentration; thus, this calculational method is used in Chapter 3. First, we relax all atoms to find the optimized structure. We consider a small atomic displacement of 0.05 Å about their equilibrium positions so that the potential energy around the equilibrium geometry can be expanded in a Taylor

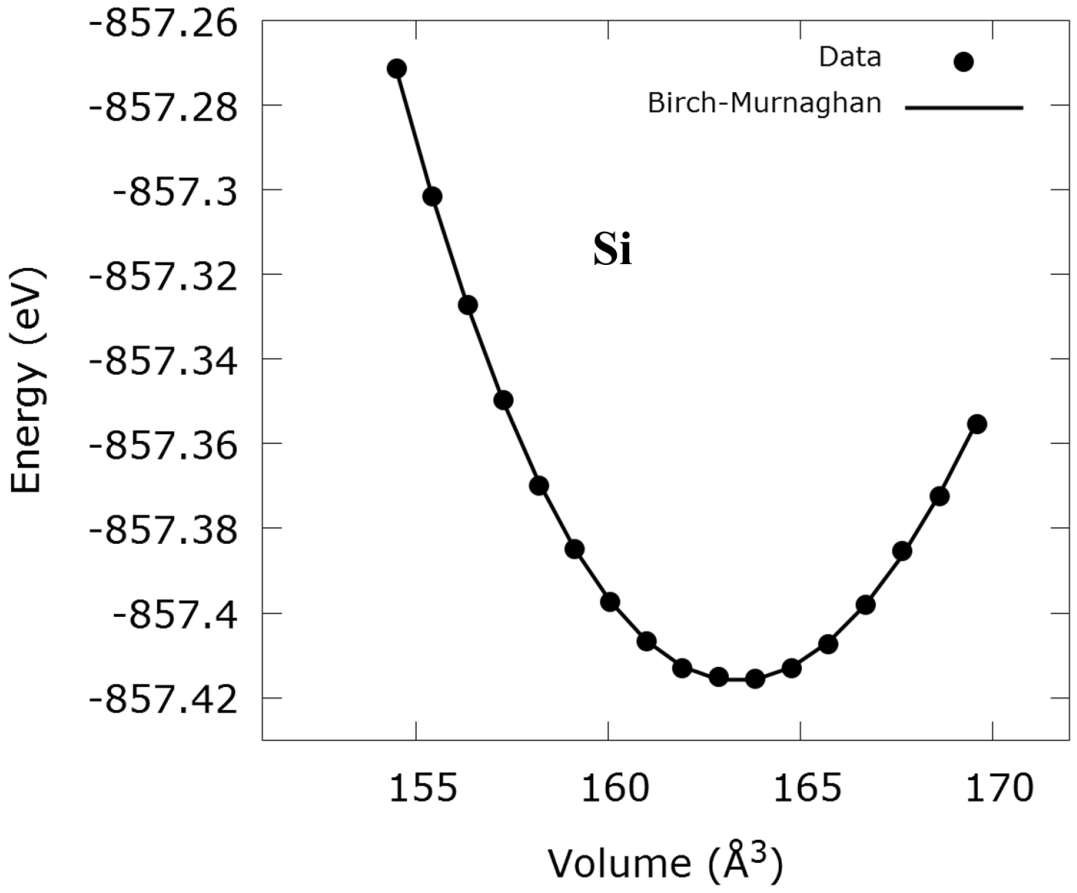

FIGURE 2.2: Volume optimization to estimate the lattice constant of silicon by using the Birch-Murnaghan equation of states. Closed-circles and solid lines are the input data and the curve model, respectively.

series. The Taylor expansion around minimum at x_0 is given by

$$E(x) = E(x_0) + \left[\frac{\partial E(x)}{\partial x_i}\right]_{x_0} x_i + \frac{1}{2!}\left[\frac{\partial^2 E(x)}{\partial x_i \partial x_j}\right]_{x_0} x_i x_j + \frac{1}{3!}\left[\frac{\partial^3 E(x)}{\partial x_i \partial x_j \partial x_k}\right]_{x_0} x_i x_j x_k + ..., \tag{2.88}$$

The linear term (second term) describes forces on all atoms. In the equilibrium geometry, these forces are zero; thus, the linear term vanishes. Since the atomic displacement is small, the contribution of the cubic and higher terms is considered to be small and thus we neglect these terms. Therefore, Eq. (2.88) reduces to the

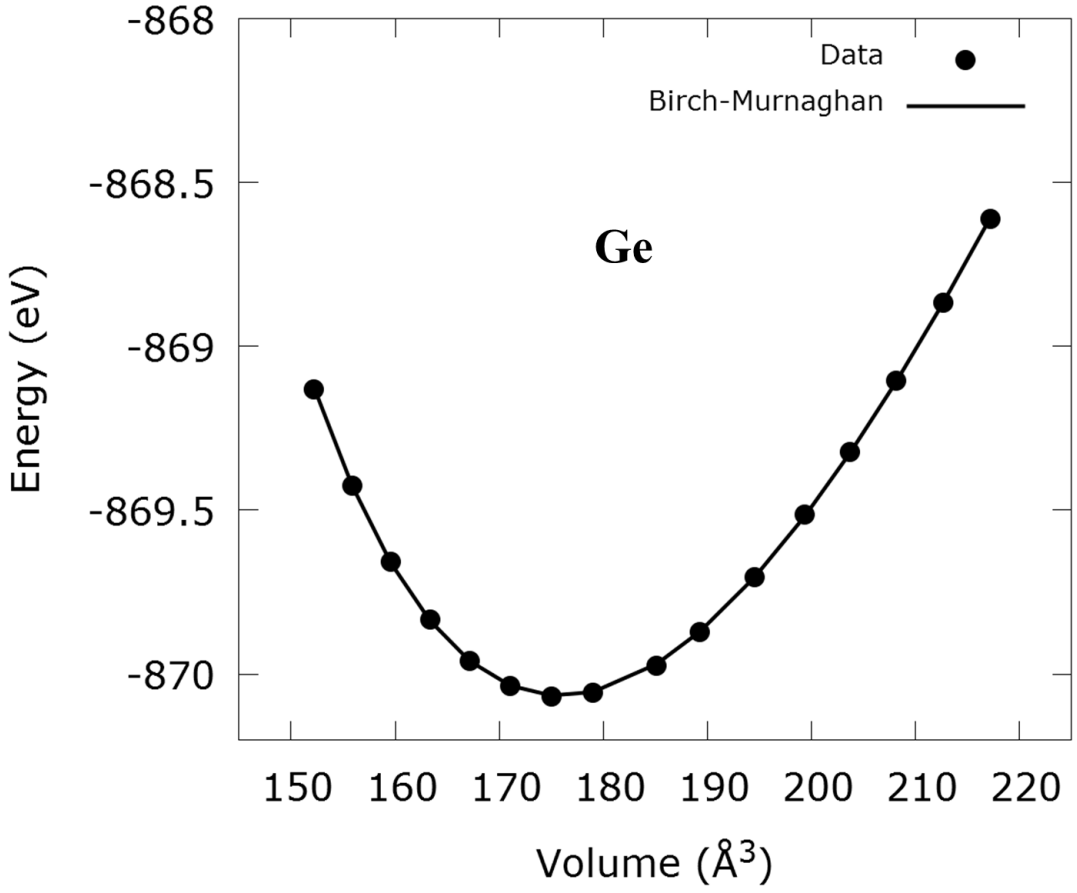

FIGURE 2.3: Volume optimization to estimate the lattice constant of germanium by using the Birch-Murnaghan equation of states. Closed-circles and solid lines are the input data and the curve model, respectively.

harmonic approximation given by

$$E(x) \approx E(x_0) + \frac{1}{2!}\left[\frac{\partial^2 E(x)}{\partial x_i \partial x_j}\right]_{x_0} x_i x_j. \tag{2.89}$$

In one dimension, the force acting on the atom in any system is given by

$$F(x) = -\left[\frac{\partial E(x)}{\partial x}\right]. \tag{2.90}$$

Considering the equation of motion of a spring system, we can express the harmonic approximation (Eq. (2.89)) as

$$F(x) = -\left[\frac{\partial E(x)}{\partial x}\right] = -k\triangle x, \tag{2.91}$$

where $k = \left[\frac{\partial^2 E(x)}{\partial x^2}\right]_{x_0}$ is the spring constant. Integrating Eq. (2.91) over x gives the potential of the harmonic oscillator, which is expressed as:

$$E(x) = E(x_0) + \frac{k}{2}(\triangle x)^2, \tag{2.92}$$

In three dimensions, the equation of motion corresponding to Eq. (2.89) is

$$m_\tau \ddot{\mathbf{u}}_\tau = -\sum_{\tau'} \Phi_{\tau,\tau'} \mathbf{u}_{\tau'}, \tag{2.93}$$

where m and u_τ are mass of atom and the displacement vector, respectively. The label $\tau = (i, \alpha), \tau' = (j, \beta)$ refers to an atom i and the cartesian components $\alpha, \beta = x, y, z$. For a supercell consisting of N atoms in three dimensions, τ runs from 1 to $3N$, and Φ is a $3N \times 3N$ matrix. $\Phi_{\tau,\tau'}$ is the second derivative of the potential energy, which is called the force constant matrix, given by

$$\Phi_{\tau,\tau'} = \frac{\partial^2 \mathbf{E}(r)}{\partial u_\tau \partial u_{\tau'}}. \tag{2.94}$$

where $\mathbf{E}(r)$ is the potential energy in 3D, which is given by

$$\mathbf{E}(r) = \mathbf{E}_0 + \frac{1}{2}\sum_{\tau}\sum_{\tau'} \Phi_{\tau,\tau'} \mathbf{u}_\tau \mathbf{u}_{\tau'}, \tag{2.95}$$

Corresponding to Eq. (2.90) we get

$$\Phi_{\tau,\tau'} = -\frac{\partial \mathbf{F}_\tau}{\partial \mathbf{u}_{\tau'}} \approx -\frac{\mathbf{F}_\tau(\triangle \mathbf{u}_{\tau'})}{\triangle \mathbf{u}_{\tau'}} \tag{2.96}$$

Eq. (2.96) can be solved numerically, and we use the central difference approximation, which is given by

$$\frac{\partial \mathbf{F}_\tau}{\partial \mathbf{u}_{\tau'}} = \frac{\mathbf{F}_\tau|_{\mathbf{u}_{\tau=a}} - \mathbf{F}_\tau|_{\mathbf{u}_{\tau'=-a}}}{2a}. \tag{2.97}$$

where a is the displacement parameter.

Next, we change varibale by setting $\mathbf{w}_\tau = \mathbf{u}_\tau/\sqrt{m_\tau}$ to make the system of equations symmetric; Eq. (2.93) is then given by

$$\ddot{\mathbf{w}}_\tau = -\sum_{\tau'} \mathbf{D}_{\tau,\tau'} \mathbf{w}_{\tau'}, \tag{2.98}$$

Assuming the solution of Eq. (2.98) is $w_\tau = Q\zeta_\tau \exp(i\omega t + \delta)$, we get

$$\omega^2 \zeta_\tau = \sum_{\tau'} \mathbf{D}_{\tau,\tau'} \zeta_{\tau'}, \tag{2.99}$$

where $\mathbf{D}_{\tau,\tau'} = \Phi_{\tau,\tau'}/\sqrt{m_\tau m_{\tau'}}$ is called *dynamic matrix*. Eq. (2.99) is the homogeneous linear system of equations with eigenvalues ω^2 and eigenvectors ζ. From the eigenvalue problem, the solution of Eq. (2.99) must satisfy the following:

$$det\left(\frac{\Phi_{\tau,\tau'}}{\sqrt{m_\tau m_{\tau'}}} - \omega^2\right)\hat{\mathbf{e}} = 0. \tag{2.100}$$

Therefore, the square of the vibrational frequencies ω^2 are the eigenvalues of the *dynamic matrix* $\mathbf{D}_{\tau,\tau'}$. The vibrational frequencies are found by diagonalizing the *dynamic matrix* whose elements are obtained from the numerical calculations of Eq. (2.97).

2.2.3 Phonon density of states

The calculated vibrational frequencies are then used to calculate the phonon density of states (DOS). The calculation of DOS is conducted to evaluate whether the softening of the vacancy system of the silicon monovacancy appears. Thus, this calcaulation is used in Chapter 3. The DOS is computed by introducing Gaussian

broadening obtained from the Gaussian integral, which is given by

$$\begin{aligned} G(x) &= \int_{-\infty}^{\infty} \exp\left(-x^2\right) dx \\ &= \sqrt{\pi}. \end{aligned} \tag{2.101}$$

The Gaussian distribution function is defined as:

$$P(x) = A \exp\left[-\frac{1}{2}\left(\frac{x-\nu}{\sigma}\right)^2\right]. \tag{2.102}$$

Normalizing Eq. (2.102) and using Eq. (2.101), one gets $A = \frac{1}{\sigma\sqrt{2\pi}}$, and the normalized Gaussian distribution function is given by

$$N(x) = \frac{1}{\sigma\sqrt{2\pi}} \exp\left[-\frac{1}{2}\left(\frac{x-\nu}{\sigma}\right)^2\right]. \tag{2.103}$$

We then introduce the DOS as follows:

$$D(E) = \sum_{i,j} \frac{1}{\sigma\sqrt{2\pi}} \exp\left[-\frac{1}{2}\left(\frac{E_i - h\nu_j}{\sigma}\right)^2\right], \tag{2.104}$$

where ν is the vibrational frequencies and σ is a parameter, which is related to the "full width at half maximum" (FWHM). i and j run over parameter x and the vibrational modes, respectively.

The FWHM is found from the half-maximum point x_h as follows:

$$\frac{1}{\sigma\sqrt{2\pi}} \exp\left[-\frac{1}{2}\left(\frac{x_h-\nu}{\sigma}\right)^2\right] = \frac{1}{2} f(x_{max}). \tag{2.105}$$

Since $f(x_{max})$ is found at $x_{max} = \nu$, one gets

$$\begin{aligned} \frac{1}{\sigma\sqrt{2\pi}} \exp\left[-\frac{1}{2}\left(\frac{x_h - \nu}{\sigma}\right)^2\right] &= \frac{1}{2} f(\nu) \\ &= \frac{1}{2}\frac{1}{\sigma\sqrt{2\pi}} \\ \exp\left[-\frac{1}{2}\left(\frac{x_h - \nu}{\sigma}\right)^2\right] &= \frac{1}{2}. \end{aligned} \tag{2.106}$$

Solving on x_h we get $x_h = \pm\sigma\sqrt{2\ln 2} + \nu$. The FWHM is then given by

$$\text{FWHM} = x_+ - x_- = 2\sigma\sqrt{2\ln 2}. \tag{2.107}$$

In the DOS calculation, we use FWHM = 80 cm^{-1}.

Chapter 3

Vibrational Effect on the Concentration of the Silicon Monovacany

3.1 Introduction

The study of point defects in semiconductors has attracted much attention because of the crucial effects of such defects on various properties of materials. Some defects capture carriers and affect the electrical conductivity of semiconductors. Therefore, control of defects is necessary for device fabrication [3].

The silicon vacancy is a fundamental defect and has been extensively investigated theoretically [3–6, 44–47] and experimentally [7–11]. Electron paramagnetic resonance (EPR) measurement has clarified the Jahn-Teller effect that lowers the symmetry from T_d [7]. Theoretical studies based on the density functional theory (DFT) show the symmetry of D_{2d} for the neutral charge state [3–5, 45–47]. Negative-U behavior was examined by experimental [48] and theoretical studies [49].

The formation of defects depends on crystal growth rate [50]. Vacancies are created at high crystal growth rates, whereas interstitials are created at low crystal growth

rates. At high temperatures up to the melting point, a finite vacancy concentration is observed in thermal equilibrium [51]. The formation energy of the monovacancy is estimated to be 3.1 – 4.1 eV in some experimental studies [8–11].

Recently, Goto *et al.* [12] have observed elastic softening at a very low temperature by ultrasonic measurements. They found the elastic softening below 20 K. Their analysis leads to the conclusion that the softening is induced by high-symmetry (T_d) defects, and they considered that the softening originates from the monovacancy. However, the defects observed by them might be different from the monovacancy examined in previous studies [13, 14]. Goto *et al.* supposed that the concentration deduced from the results of a low-temperature experiment is the same as that of the thermal equilibrium monovacancy near the melting point; therefore, the concentration near the melting point should be clarified.

In this study, we carry out a large-scale first-principles calculation to accurately estimate the concentration of the monovacancy. We use large supercells containing 1728 and 216 sites for calculating formation energy and the vibrational effect on the concentration of the monovacancy, respectively. The calculations are much larger than those in previous studies; i.e., up to 1000-site supercell calculation for the formation energy and up to 64-site supercell calculation for the vibrational effect have been carried out thus far [3–6, 46, 52, 53]. By using large supercells, we confirm good convergence. We expect that the vibrational effect significantly contributes to the increase in the concentration of the monovacancy and thus the calculation without the vibrational effect is not reliable.

3.2 Computational Details

To simulate defects, we use supercell models (see Fig. 3.1) containing 64, 216, 512, 1000, and 1728 atomic sites. We remove one atom from supercells and then allow all remain atoms to relax so that the atomic force is less than 5×10^{-2} eV/Å. Γ-point and Monkhorst-Pack grid (k_{MP}) [54] are carried out in the Brillouin zone integration. The use of supercell models efficiently reduces computational cost; however, it introduces an error, which is due to defect-defect image interactions

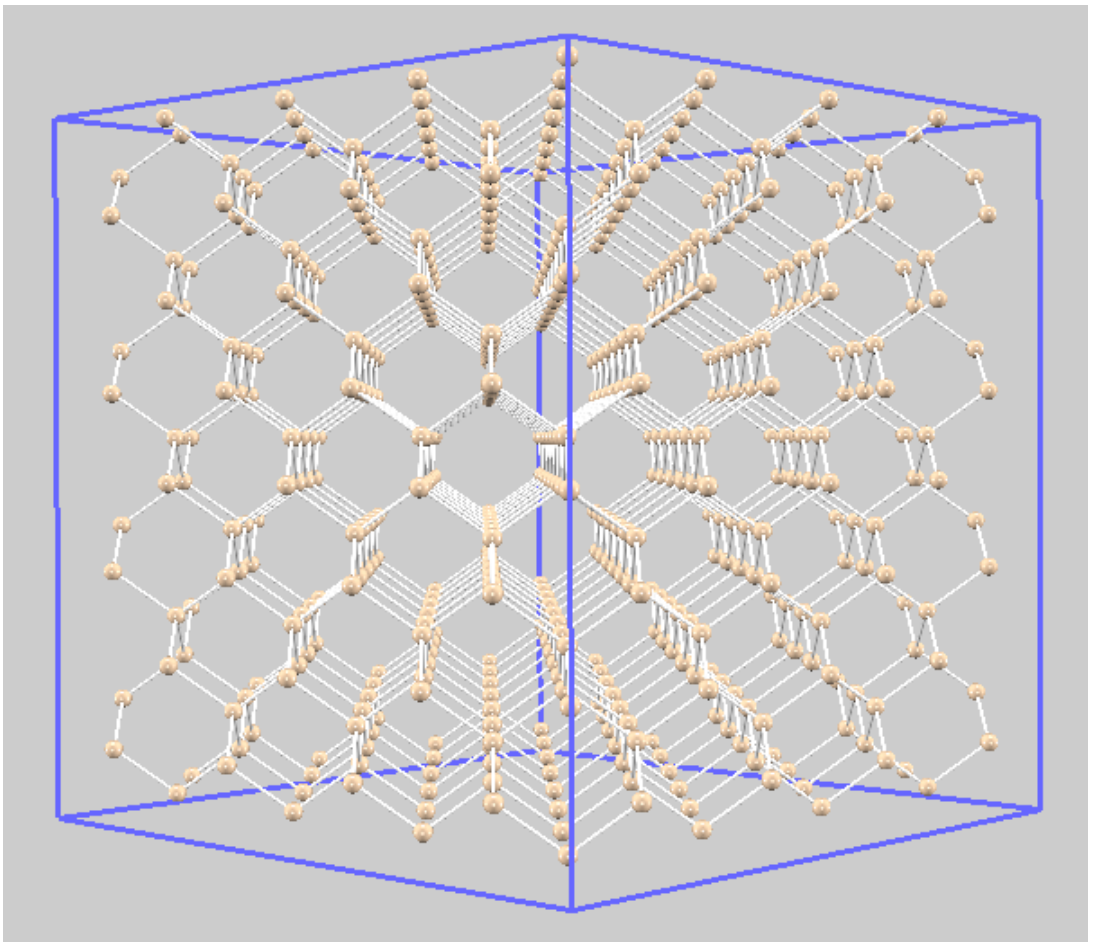

FIGURE 3.1: Supercell containing 512 atomic sites, which is generated from a $4 \times 4 \times 4$ times 8-sites unit cell.

[4, 55–57]. The error decreases as the supercell size increases. Thus, a larger supercell gives more accurate results of electronic properties such as formation energy.

The formation energy (E^f) of a neutral vacancy is calculated as [3, 5]

$$E^f = E^v_{N-1} - (\frac{N-1}{N})E_N, \tag{3.1}$$

where E_N is the total energy of the perfect supercell consisting of N atoms and E^v_{N-1} is the total energy of the supercell for the monovacancy. By using the

formation energy, the concentration of the vacancy is roughly approximated by [8]

$$C_0 = N_0 \exp(-\frac{E^f}{k_B T}), \tag{3.2}$$

where N_0, k_B, and T are the total number of atoms per unit volume, Boltzmann constant, and temperature, respectively. However, when the vibrational effect and configurational entropy are considered, the concentration is given by [46]

$$C_S = C_0 n_c \exp(-\frac{F^f_{vib}}{k_B T}), \tag{3.3}$$

where n_c is the number of geometries with the lowest energy. A neutral vacancy has the D_{2d} symmetry, $n_c = 3$, which gives the formation configurational entropy $S^f_c = 1.1 k_B$. F^f_{vib} is the formation vibrational free energy given by [46]

$$F^f_{vib} = F^v_{vib} - (\frac{N-1}{N}) F^p_{vib}, \tag{3.4}$$

where F^v_{vib} and F^p_{vib} are the vibrational free energies of the vacancy and perfect crystal, respectively. These vibrational free energies are given by [46, 58]

$$F_{vib} = k_B T \sum_i \ln[\sinh(\frac{h\nu_i}{2k_B T})], \tag{3.5}$$

where h is Planck's constant and ν is the vibrational frequency. i runs over the vibrational modes.

The formation vibrational entropy S^f_{vib} is given by [59]

$$S^f_{vib} = S^v_{vib} - (\frac{N-1}{N}) S^p_{vib}, \tag{3.6}$$

where S^v_{vib} and S^p_{vib} are the vibrational entropies of the vacancy and perfect crystal, respectively, which can be calculated from the first derivative of F_{vib} over temperature [58]:

$$S_{vib} = -\left(\frac{\partial F_{vib}}{\partial T}\right)_V. \tag{3.7}$$

In the above calculation of the vacancy concentration in Eq. (3.3), we need to

evaluate the vibrational frequencies. Thus, the second derivatives of the energy over atomic coordinates are computed numerically within the harmonic approximation, i.e., the second derivatives are estimated from the atomic force for the geometry where the atom is in a displaced position. We consider an atomic displacement of 0.05 Å in this calculation. The vibrational frequencies are obtained by diagonalizing the dynamical matrix whose elements are calculated from the second derivatives. The detail explanation of the calculation of the vibrational frequencies was previously given in Chapter 2.

3.3 Results and Discussion

3.3.1 Formation energy

We calculate the formation energy and concentration of the silicon neutral monovacancy $V_{S_i}^0$. The initial geometry of the unrelaxed monovacancy has the T_d symmetry. During relaxation, Jahn-Teller effect lowers the symmetry from T_d. We find that the most stable geometry of the vacancy has the D_{2d} symmetry for all supercells. The results are in agreement with those of previous theoretical calculations [3–6, 44]. The symmetry lowering from T_d to D_{2d} is explained in Appendix A.

In the D_{2d} geometry, four nearest-neighboring atoms form two pairs, as shown in Fig. 3.2. The two distances between the nearest-neighboring atoms are denoted by L_1 and L_2 ($L_1 > L_2$), which are shown in Table 3.1. The calculated volume of the tetrahedron, whose top is placed at a nearest-neighbor site, is smaller than that of the ideal one (Table 3.1). This volume reduction originates from the inward relaxation of the nearest-neighbor atom.

We plot the displacement of atoms from the ideal position in Fig. 3.3. As the distance from the vacancy center increases, the displacement tends to decrease. In the 1728-site cell, the displacement of the atoms, which are more than 9.2 Å from the vacancy center, is very small (less than 0.005 Å), expecting that the 1728-sites

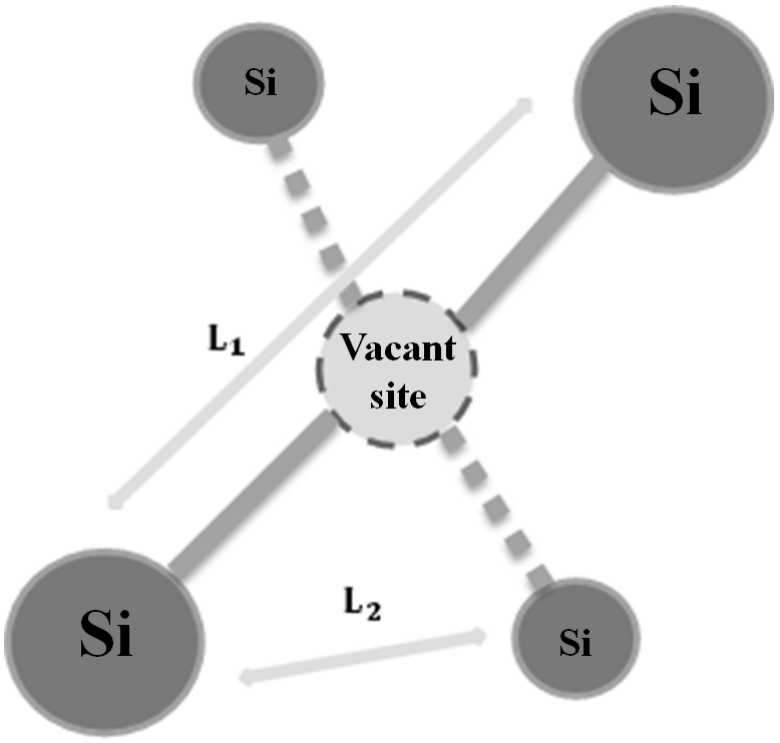

FIGURE 3.2: Geometry of the neutral vacancy: four nearest-neighboring atoms of the vacancy form two pairs. L_1 and L_2 are the distances between two atoms, where $L_1 > L_2$.

supercell-size is large enough and giving a converged value of the formation energy.

We calculate the formation energy using supercells whose sizes are up to 1728 atomic sites. As shown in Table 3.1, for the 64- and 216-atomic-sites supercells, Γ-point produces both D_{2d} and T_d symmetries. The T_d symmetry has higher formation energy by 0.19 and 0.40 eV for the 64- and 216-atomic sites, respectively. However, when $k_{MP} = 8$ and $k_{MP} = 64$ are used as k-point Brillouin-zone sampling, the optimized geometry tends to have the D_{2d} symmetry. This indicates that the geometry having the T_d symmetry is less stable compared with that having the D_{2d} symmetry, and thus D_{2d} is considered as the ground state of the system. Moreover, the 512 – 1728-atomic-sites supercells produce the D_{2d} symmetry, which also indicate that the most stable geometry of the silicon monovacancy has the D_{2d} symmetry.

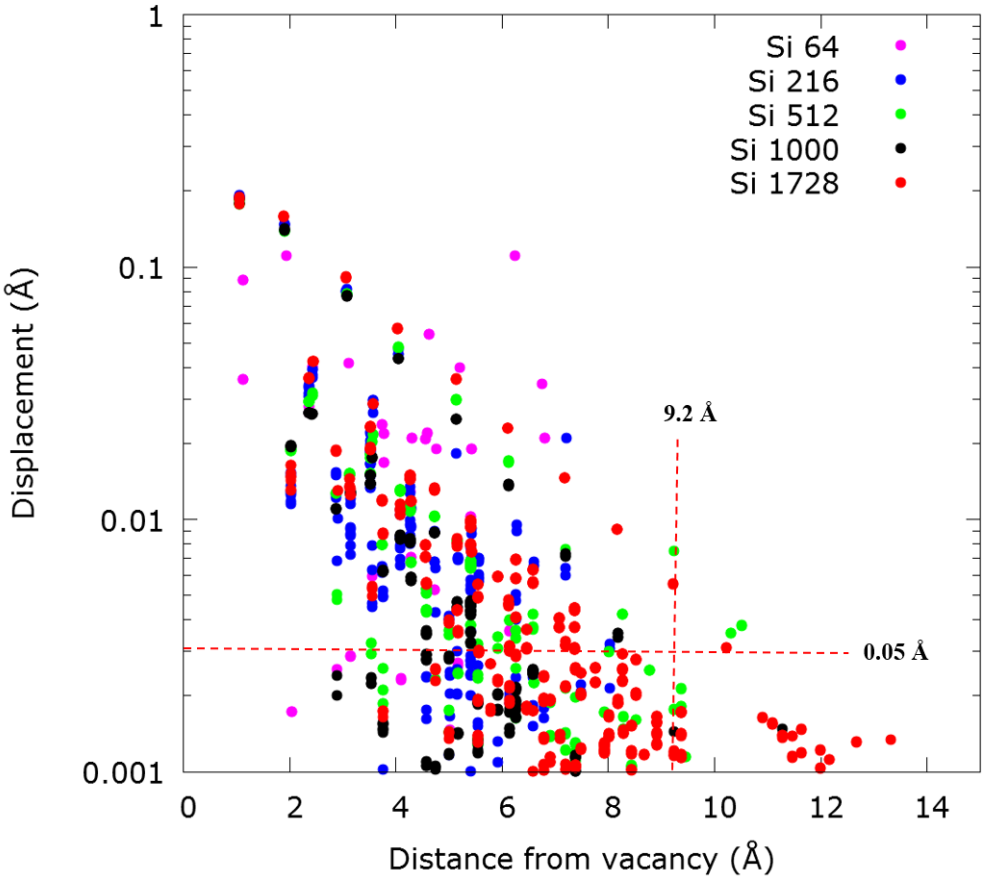

FIGURE 3.3: Displacements of atoms from the ideal position as a function of the distance from the vacancy.

To minimize the defect-defect image interactions appearing from the use of the supercell model, we use large supercell whose size is 1728 atomic sites, and we confirm the convergence with respect to the cell size. The formation energy well converges when a 1728-atomic-site supercell is used (Table 3.1). The difference between the formation energies calculated from 1000- and 1728-site supercells is very small (0.02 eV). We next confirm the convergence by decreasing the atomic force from 5 $\times 10^{-2}$ eV/Å to 2 $\times 10^{-3}$ eV/Å in the 1728-sites calculation and we find that the formation energy difference is very small (0.003 eV). Therefore, our calculated value (3.46 eV) well converges and is close to the experimental values.

Dannefaer *et al.* [8] carried out the positron annihilation experiment and estimated the formation energy to be 3.6 ± 0.2 eV. Watkins and Corbett [9] estimated

TABLE 3.1: Results of supercell calculations. V_r is the defect volume change defined as $V_r = (V\text{-}V_0)/V_0$, where V and V_0 are the volumes of the tetrahedra formed by the four nearest-neighboring atoms of the relaxed and ideal vacancies, respectively [52]. L_1 and L_2 are distances between the nearest-neighboring atoms in the relaxed geometries (see Fig. 3.2). The ideal (unrelaxed) bulk distance and defect volume are 3.87 Å and 6.81 Å^3, respectively. E^f is the formation energy and N is the supercell size.

N	k-point	V_r (%)	L_1 (Å)	L_2 (Å)	Symmetry	E^f (eV)
64	Γ	-30.75	3.60	3.16	D_{2d}	3.05
	Γ		3.72	3.72	T_d	3.24
	8		3.57	3.47	D_{2d}	3.48
	64		3.59	3.47	D_{2d}	3.65
216	Γ	-43.00	3.44	2.90	D_{2d}	3.31
	Γ		3.46	3.46	T_d	3.71
	8		3.48	2.96	D_{2d}	3.52
512	Γ	-42.29	3.43	2.94	D_{2d}	3.43
1000	Γ	-42.72	3.42	2.94	D_{2d}	3.48
1728 [a]	Γ	-44.08	3.44	2.87	D_{2d}	3.46(3)
1728 [b]	Γ		3.44	2.89	D_{2d}	3.46(0)

[a] atomic force = 5 $\times 10^{-2}$ eV/Å
[b] atomic force = 2 $\times 10^{-3}$ eV/Å

the formation energy to be 3.6 ± 0.5 eV from the EPR experiment. Shimizu *et al.* [10] estimated the formation energy to be $3.6^{+0.3}_{-0.1}$ eV from the Raman shift measurement. Fukata *et al.* [11] used a quenching method and estimated the formation energy to be about 4.0 eV. These results are consistent with the present value.

The previous theoretical calculations that used 64 – 1000-atomic-site supercells show that the formation energies are 3.0 – 4.1 eV [3–6, 52, 53], which are close to our value. The 1000-site calculation based on the GGA [4] gives a value of 3.62 eV, which is close to the present value from the 1728-site calculation (3.46 eV). A

recent 512-site calculation based on the Heyd-Scuseria-Ernzerhof screened hybrid functional [53] gives a formation energy of 4.08 eV.

3.3.2 Vacancy concentration

We next calculate the vibrational frequencies by using a 216-site supercell. In this calculation, we use relaxed atomic positions of the vacancy system and displace each atom 0.05 Å from their equilibrium positions. The vibrational frequencies are computed numerically by using the harmonic approach. The calculated vibrational frequencies over the number of modes are shown in Fig. 3.4.

The density of states (DOS) is computed by introducing Gaussian broadening (Eq. (2.103)) whose half-width is 50 cm^{-1} (Fig. 3.5). Comparing the DOS of the vacancy system with that of the perfect system, we find that the vibrational frequencies are lower in the vacancy case. This softening of the vacancy system is expected to increase the vacancy concentration.

Next, the monovacancy concentration is calculated. The concentration as a function of temperature is given in Fig. 3.6. We use the formation energy estimated from the 1728-site cell calculation and calculate vibrational frequencies by using the 64- and 216-site supercells. At the melting point (1685 K), C_S in Eq. (3.3) is estimated to be 8.2×10^{16} and 7.4×10^{16} cm^{-3} by using the 64- and 216-site supercell calculations, respectively. Thus, the result is insensitive to the supercell size used in the calculation of vibrational frequencies. C_0 in Eq. (3.2) is estimated to be 2.2×10^{12} cm^{-3}, which is much lower than C_S, by considering the vibrational effect and configurational entropy. The high C_S value is mainly due to the fact that the vibrational frequencies are softened in the vacancy system. The configurational entropy effect increases the concentration only three times, and thus the entropy only slightly affects the concentration.

The formation vibrational entropy as a function of temperature is given in Fig. 3.7. The entropy converges at 1100 K, giving a value of $9.1k_B$. At the melting point, the S^f_{vib} values calculated from the 64- and 216-site supercells are $9.3k_B$ and

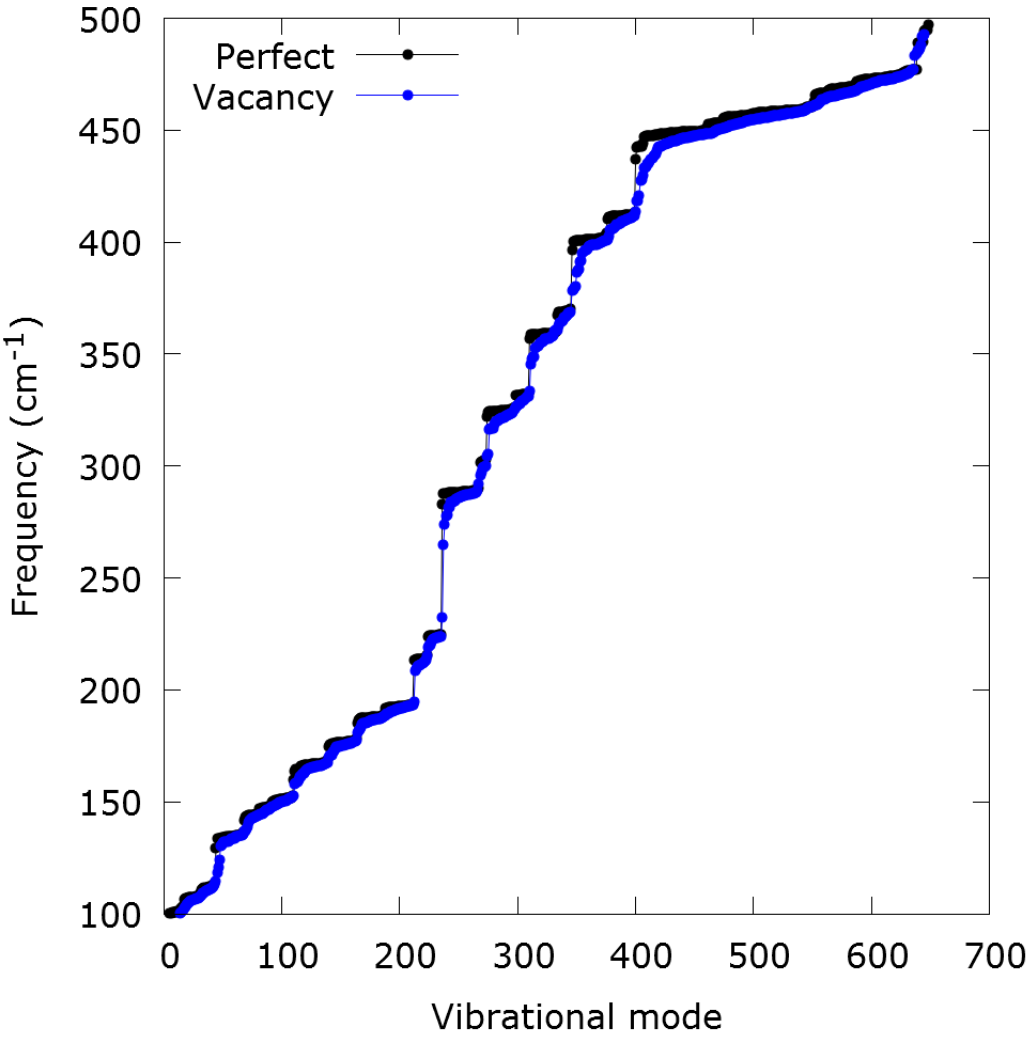

FIGURE 3.4: Vibrational frequency for each mode calculated from the perfect supercell (black) and its vacancy system (blue).

$9.1k_B$, respectively. Thus, the sum of the vibrational and configurational entropies is $\sim 10k_B$.

From a positron annihilation study, Dannefaer *et al.* [8] estimated the vacancy concentrations to be 10^{14} – 10^{16} cm^{-3} at 1500 K [51]. At this temperature, we estimate the concentration to be 4.0×10^{15} cm^{-3}, which shows very good agreement with their estimations. At the melting point (1685 K), Voronkov and Falster [60] obtained a vacancy concentration of 10^{15} cm^{-3} by analyzing experimental results of boron doping [61]. Our calculated value (7.4×10^{16} cm^{-3}) is somewhat

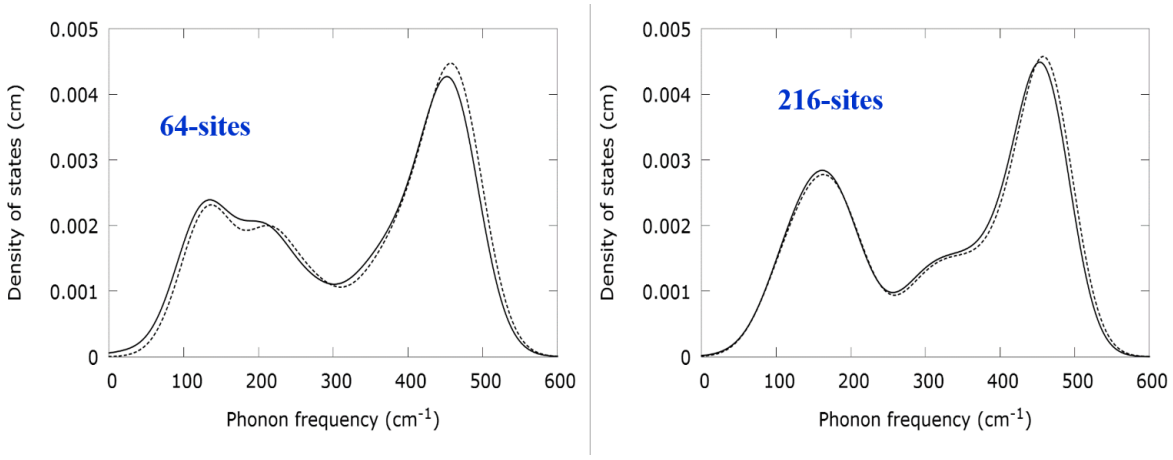

FIGURE 3.5: Vibrational density of states calculated from the 64-sites (left) and 216-sites (right) supercells for vacancy system (solid line) and perfect system (dashed line).

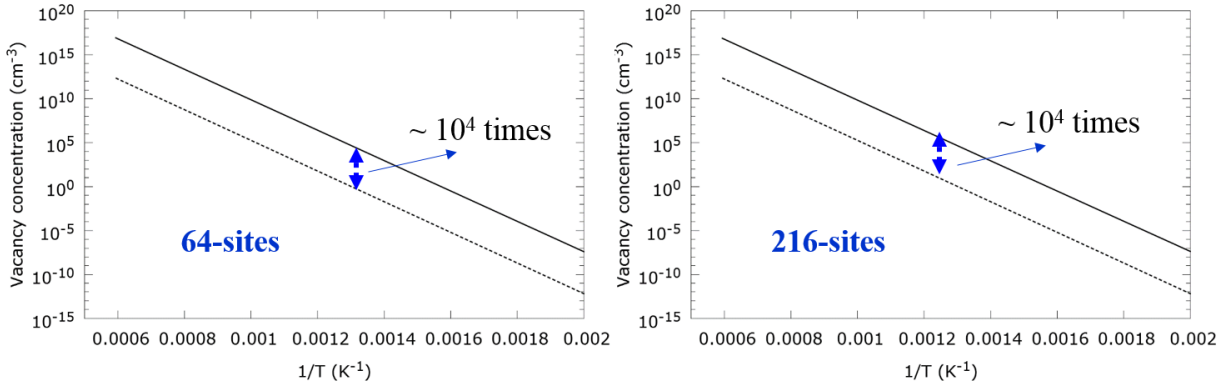

FIGURE 3.6: Vacancy concentration as a function of inverse temperature calculated from the 64-sites (left) and 216-sites (right) supercells. Calculations of C_S (solid line) and C_0 (dashed line) are carried out by using Eqs. (3.3) and (3.2), respectively.

higher. The small deviation may come from the use of a different formation energy (Voronkov and Falster used the value of 4.5 eV).

Goto *et al.* [12] detected a defect by low-temperature ultrasonic measurement and considered that the detected defect is a monovacancy. By analyzing the results of the low-temperature experiment, they estimated the concentration to be 10^{15} cm^{-3} and expected that the concentration would be the same as that at the melting point. Their estimated concentration is only slightly lower than our present value at the melting point (7.4×10^{16} cm^{-3}). Thus, this seems to

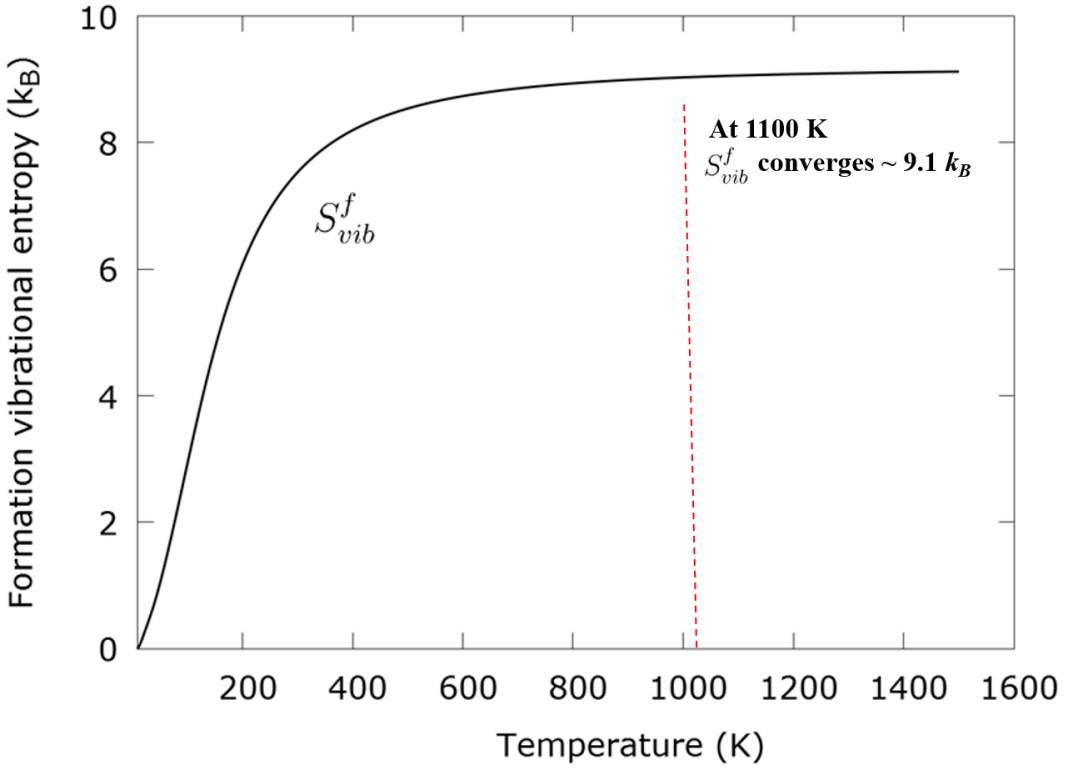

FIGURE 3.7: Formation vibrational entropy (S^f_{vib}) in Eq. (3.6) as a function of temperature.

support their expectation. However, it should be noted that monovacancies likely agglomerate in cooling specimens as argued in Ref. 19. If so, the detected defect is not a monovacancy.

Lannoo and Allan calculated the vibrational entropy using Green's-function technique and obtained a vibrational entropy value of $6k_B$ or more [62, 63]. Using the same technique, Leite *et al.* calculated a 17-atom cluster and showed that the vibrational entropy can reach $10k_B$ [64]. Al-Mushadani and Needs conducted a DFT calculation based on the local density approximation (LDA) using 64 atomic sites and obtained a vibrational entropy of about 1×10^{-3} eVK^{-1} ($12k_B$) and a vacancy concentration of 10^{16} cm^{-3} at 1500 K [46]. Our calculated vibrational entropy value is $9.1k_B$ and the vacancy concentration is 4.0×10^{15} cm^{-3}. These values are close to the theoretical results.

Chapter 4

Summary

4.1 Conclusion

We have carried out DFT calculations of $V_{S_i}^0$ by using large-scale supercells. The supercells were larger than those in the previous studies [3–6, 46, 52, 53] and we confirmed the convergence of calculational results. Therefore, we believe that the present DFT calculations give reliable results. In the 1728-site supercell calculation, we found that the displacement of the atoms, which are more than 9.2 Å from the vacancy site, is very small (less than 0.005 Å), suggesting that the calculational formation energy converges. In fact, we found that the formation energy estimated from the 1728-site supercell calculation is 3.46 eV, and we confirmed the convergence. The estimated formation energy is close to the experimental values. As for the vibrational effect, we found that the 64- and 216-site supercell calculations give similar results, indicating that the results well converge. The vacancy concentrations at 1500 and 1685 K (silicon melting point) were estimated to be 4.0 $\times$ 10^{15} and 7.4 $\times$ 10^{16} cm^{-3}, respectively, which are in good agreement with the experimental values. We found that the vibrational effect significantly increases the vacancy concentration about 10^4 times.

4.2 Future Scope

By using the DFT calculations based on quantum mechanical simulation, we get useful results. We succeed to simulate the silicon monovacancy by using a large-scale supercell. We show that the vibrational effect significantly contributes to the increase of the concentration of the silicon monovacancy. We show that the calculation without the vibrational effect is not reliable. Our results are consistent with those of the recent ultrasonic measurements [12].

In this study, we focus on the monovacancy. The study of multivacancies is important. Some configurations were proposed such as the "part of hexagonal ring" (PHR) and fourfold configurations (Fig. 4.1). In the silicon case, it was theoretically clarified that the fourfold configurations are more stable than the PHR ones [66]. A very recent deep-level transient spectroscopy (DLTS) measurement has also found that the fourfold configuration is the most stable configuration in the case of the silicon trivacancy [67]. In the germanium case, we carry out calculations of multivacancies whose sizes are $1 \leq N_v \leq 6$. We clarify the stability of the vacancies in germanium and show prominent differencess between the silicon and germanium vacancies. We present the detail results in Appendix B. This study opens the future research of defects in semiconductors such as the DLTS and EPR studies to confirm these results.

For further study, we would like to apply this calculation scheme in other materials such as carbon and SiC (silicon carbide) having the same diamond-structure. The investigation of the vacancy concentration and the clarification of the most stable configurations in such materials would give useful guidance in understanding the defects properties in such materials.

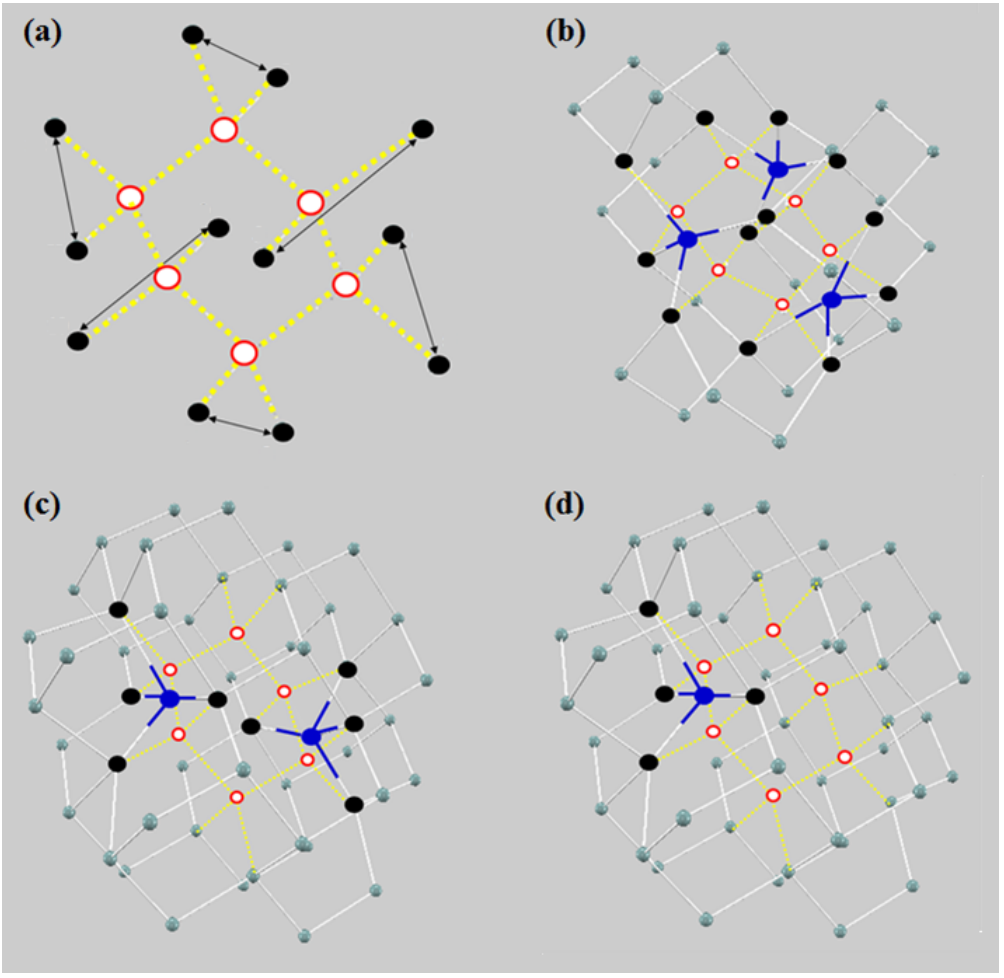

FIGURE 4.1: The hexavacancy forming a hexagonal-ring configuration is shown in (a). The fourfold configurations of the tri-, tetra-, and penta-vacancies are shown in (b), (c) and (d), respectively. Red open-circles represent vacancies, and blue and black closed-circles do interstitial atoms and their nearest-neighboring atoms, respectively.

Appendix A

Symmetry and Group Theory

In Chapter 3, we mentioned the configuration of the monovacancy having the D_{2d} and T_d symmetries. The symmetries are determined by using group theory analysis. In this part, we explain the symmetry and group theory.

A symmetry element belongs to a molecule if the symmetry operation leaves the entire molecule atoms unchanged (identical atoms and bonds having been moved are not taken into account). A symmetry element contains a point, line or a plane with a rotation and or reflection operations. Table A.1 shows symmetry elements and their symbols and definition.

Molecules are grouped based on their symmetry. The symmetry operations in Table A.1 satisfying all of the requirements of a group belongs to a group. In general, a set of operations is addressed to a group if they follow the rules below. Let we have elements **A**, **B**, and **C**. They form a group **G** if satisfies four axioms as follows:

1. (Closure) If **A** and **B** are members of **G**, then the product **A** • **B** must also be a member of **G**.

2. (Identity) There is an identity element **E** such that any elemenent **A** of **G** satisfies **E** • **A**=**A** • **E**=**A**.

TABLE A.1: Symmetry operation and its elements and symbols.

Symbol	Element	Symmetry operation
E		Identity
C_n	n-fold axis	Rotation by $2\pi/n$
σ	Mirror plane	Reflection
i	Center of inversion	Inversion
S_n	n-fold axis of improper rotation	Rotation by $2\pi/n$ followed by reflection perpendicular to the principle axis

3. (Associativity) For all **A**, **B**, **C** in **G**, the multiplication is associative satisfying $(\mathbf{A} \bullet \mathbf{B}) \bullet \mathbf{C} = \mathbf{A} \bullet (\mathbf{B} \bullet \mathbf{C})$.

4. (Inverse) For any element **A** of **G**, there is element $\mathbf{A}^{-1}$ such that $\mathbf{A} \bullet \mathbf{A}^{-1} = \mathbf{A}^{-1} \bullet \mathbf{A} = \mathbf{E}$.

A.1 Point group

The group theory can be used to predict molecular properties such as molecular orbital and symmetry properties. Here, we focus on the point group and use it to analyze the geometry of defects and identify the point groups they belong. Atomic geometries having the same symmetry elements are collected into point group. The identification of the point group for such geometries commonly uses the character table representation. The character table representations of selected point groups are given in Table A.2 – Table A.3.

TABLE A.2: Character table representation of point group T_d.

T_d	E	$8C_3$	$3C_2$	$6S_4$	$6\sigma_d$		
A_1	1	1	1	1	1		$x^2+y^2+z^2$
A_2	1	1	1	-1	-1		
E	2	-1	2	0	0		$(2z^2-x^2-y^2, \sqrt{3}(x^2-y^2))$
T_1	3	0	-1	1	-1	(R_x, R_y, R_z)	
T_2	3	0	-1	-1	1	(x, y, z)	(xy, xz, yz)

TABLE A.3: Character table representation of point group D_{2d}.

D_{2d}	E	$2S_4$	C_2	$2C_2'$	$2\sigma_d$		
A_1	1	1	1	1	1		x^2+y^2, z^2
A_2	1	1	1	-1	-1	R_z	
B_1	2	-1	2	0	0		x^2-y^2
B_2	1	-1	1	-1	1	z	xy
E	2	0	-2	0	0	(x, y)	(xz, yz)
						(R_x, R_y)	

TABLE A.4: Character table representation of point group D_{3d}.

D_{3d}	E	$2C_3$	$3C_2$	i	$2S_6$	$3\sigma_d$		
A_{1g}	1	1	1	1	1	1		x^2+y^2, z^2
A_{2g}	1	1	-1	1	1	-1	R_z	
E_g	2	-1	0	2	-1	0	(R_x, R_y)	$(x^2-y^2, 2xy)$
								(xz, yz)
A_{1u}	1	1	1	-1	-1	-1		
A_{2u}	1	1	-1	-1	-1	1	z	
E_u	2	-1	0	-2	1	0	(x, y)	

TABLE A.5: Character table representation of point group C_{2h}.

C_{2h}	E	C_2	I	σ_h		
A_g	1	1	1	1	R_z	x^2, y^2, z^2, xy
B_g	1	-1	1	-1	R_x, R_y	xz, yz
A_u	1	1	-1	-1	z	
B_u	1	-1	-1	1	x, y	

TABLE A.6: Character table representation of point group C_2.

C_2	E	C_2		
A	1	1	z, R_z	x^2, y^2, z^2, xy
B	1	-1	x, y, R_x, R_y	yz, xz

TABLE A.7: Character table representation of point group D_3.

D_3	E	$2C_3$	$3C_2$		
A_1	1	1	1		$x^2 + y^2, z^2$
A_2	1	1	-1	y, R_z	
E	2	-1	0	(x, y) (R_x, R_y)	$(x^2 - y^2, 2xy)$ (xz, yz)

TABLE A.8: Character table representation of point group C_{2v}.

C_{2v}	E	C_2	$\sigma_v(xy)$	$\sigma'_v(yz)$		
A_1	1	1	1	1	z	x^2, y^2, z^2
A_2	1	1	-1	-1	R_z	xy
B_1	1	-1	1	-1	x, R_y	xz
B_2	1	-1	-1	1	y, R_x	yz

A.2 Jahn-Teller effect

One of applications of the point group is to analyze the symmetry breaking observed in the molecular geometry that lowers the symmetry and energy. In 1937, Hermann Jahn and Edward Teller introduced the Jahn-Teller effect by using group theory [68]. The JahnTeller effect essentially describes a geometrical distortion of molecules that reduces its symmetry. This effect is observed in the defective crystal system; i.e., the silicon and germanium monovacancies having tetrahedral shape with the T_d symmetry is geometrically distorted to the D_{2d} symmetry.

The tetrahedral shape formed by four atoms neighboring a vacancy of the silicon monovacancy has six same side lengths (Fig. A.1 (a)). It has symmetry operations of E, C_2, C_3, S_4, and σ_d, as shown in Fig. A.1 (b). Based on Table A.2, the tetrahedral shape belongs to T_d symmetry. In the optimized geometry, the six side lengths are distorted forming two pairs, one pair consists of two same side lengths, denoted by L_1, and another pair consists of four same side lengths, denoted by L_2 (Fig. A.2 (a)). This new shape has symmetry operations of E, C_2, C_2', S_4, and σ_d, as shown in Fig. A.2 (b); thus it belongs to D_{2d} symmetry. Therefore, the Jahn-Teller effect reduces the T_d symmetry to the D_{2d} symmetry. This symmetry reduction is shown by character table representation in Table A.9.

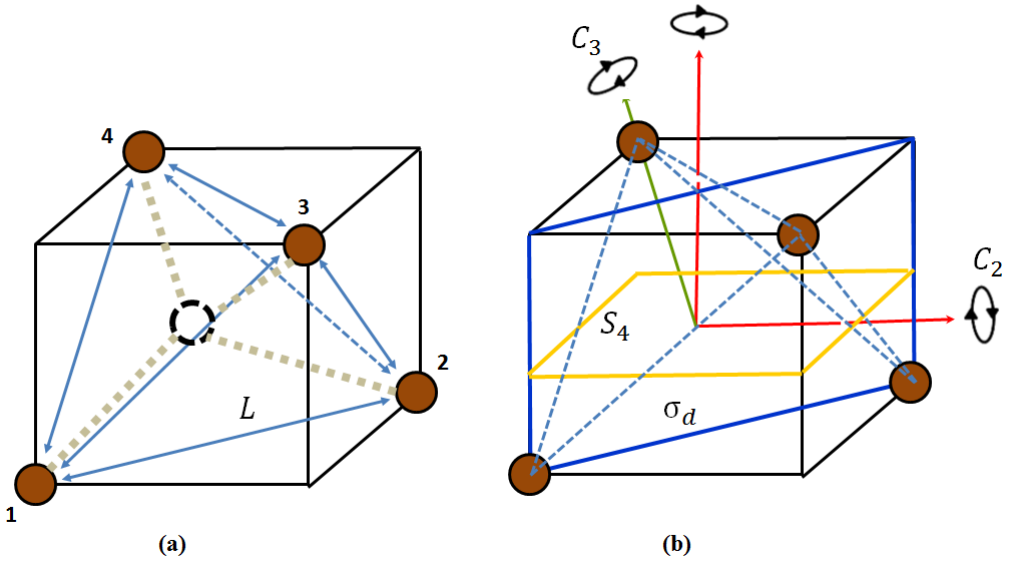

FIGURE A.1: Ideal structure of the silicon monovacancy: (a) four nearest-neighboring atoms forming a tetrahedral shape with the six same side lengths denoted by L. The vacant site is in the center. (b) symmetry operations of the T_d symmetry.

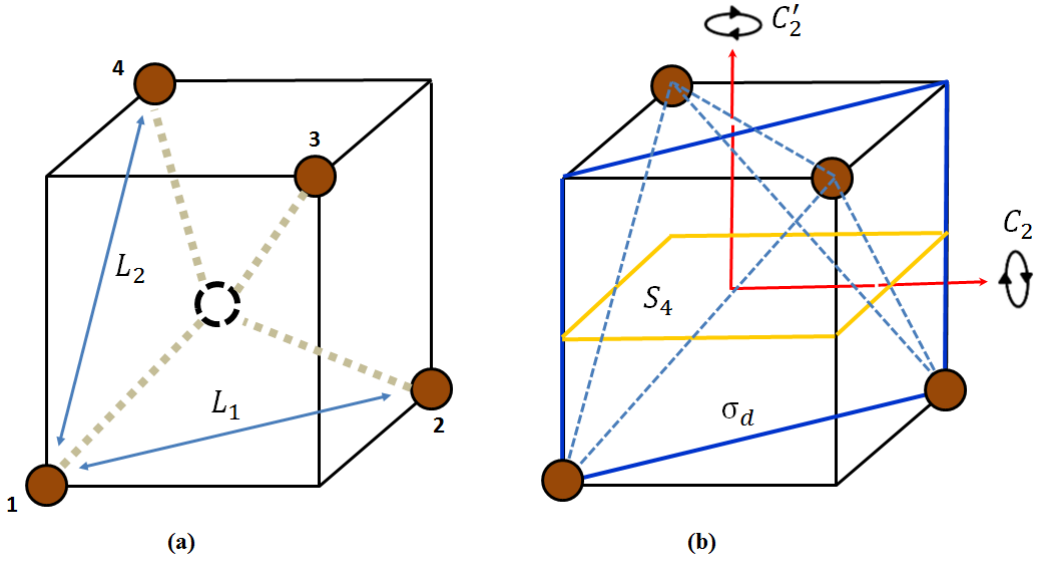

FIGURE A.2: Optimized structure of the silicon monovacancy: (a) four nearest-neighboring atoms forming a tetrahedral shape with the two side pairs denoted by L_1 and L_2. The vacant site is in the center. (b) symmetry operations of the D_{2d} symmetry.

TABLE A.9: Character table representation of the symmetry reduction from T_d to D_{2d}.

T_d	D_{2d}
A_1	A_1
A_2	B_1
E	$A_1 + B_1$
T_1	$A_2 + E$
T_2	$B_1 + E$

Appendix B

Development of the Study: Stability of the Multivacancies in Germanium

In this part, we present the calculational details and results of the multivacancies in germanium. We simulate two favorable configurations, the "part of hexagonal ring" (PHR) and fourfold configurations of the tri-, tetra-, and penta-vacancies. Next, we compare the results of germanium and silicon.

B.1 Introduction

Defects in semiconductors play important roles in fabricating semiconductor-based electronic devices because they have crucial effects on the electronic structures. Recently, germanium has attracted much attention due to its high carrier mobility as an active layer and its compatibility with silicon in electronic devices [15, 69]. Whereas defects in silicon were well studied [3, 4, 9–11, 44, 52], those in germanium are not well clarified. As for vacancies, the mono- and divacancies have been investigated theoretically [70–74] and experimentally [15, 75, 76].

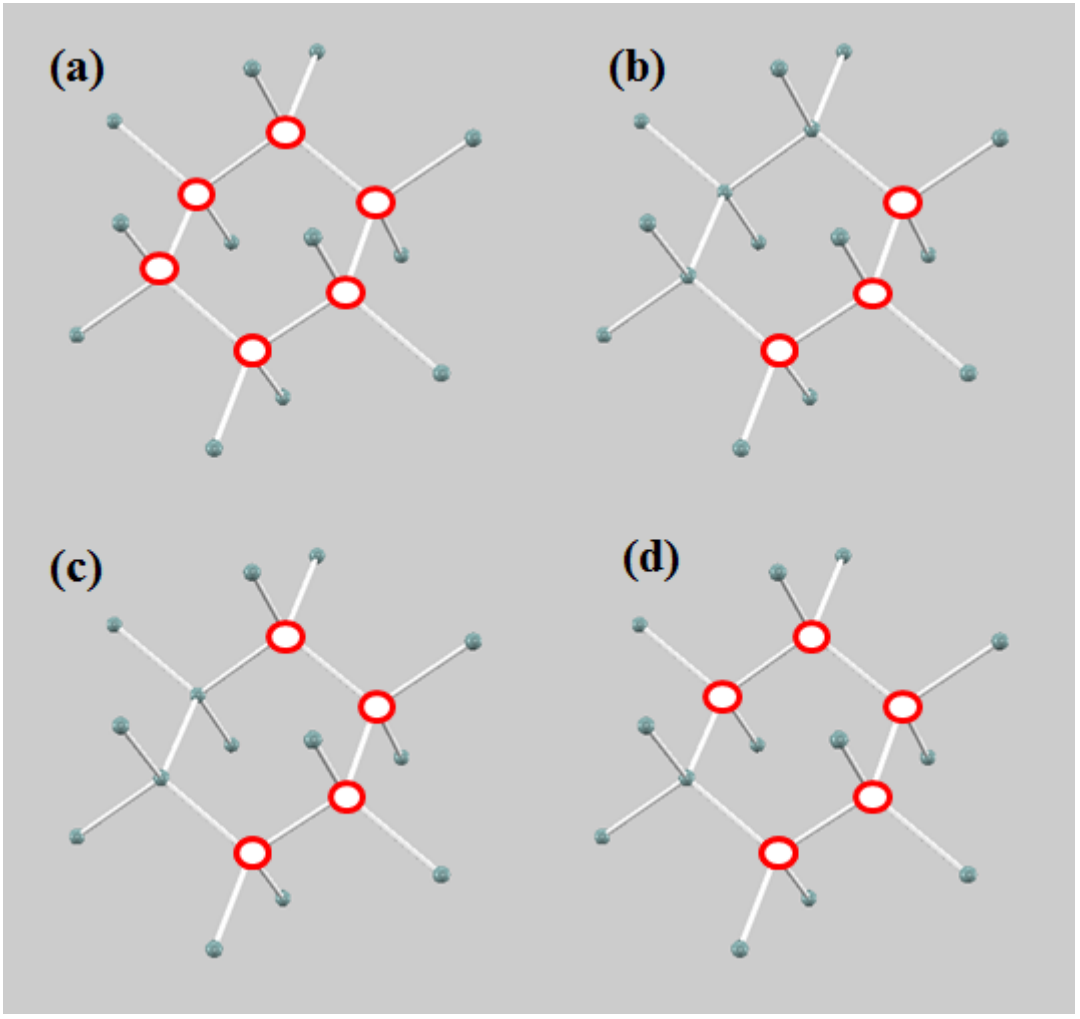

FIGURE B.1: PHR configurations. The PHR configurations of the tri-, tetra-, and penta-vacancies are shown in (b), (c), and (d), respectively, whereas the hexavacancies is shown in (a). Red open-circles are vacancies.

Magic number has been discussed for Si multivacancies [77]. The dangling bond counting (DBC) model, proposed by Chadi and Chang [77], indicates the stability of multivacancies in silicon. According to this model, the decrease of dangling bonds (broken bonds) makes the vacancies more stable. The model leads to so-called magic numbers: the numbers of missing host atoms of $n = 4m + 2$ ($m = 1, 2, 3, ...$) are energetically stable [44, 77–79]. Chadi and Chang concluded that the hexavacancy (V_6) having a hexagonal ring network of missing atoms and decavacancy (V_{10}) having a cage network are energetically stable.

The stability of the hexavacancy (Fig. B.1(a)) was also examined by using the density-functional-theory calculations [78, 80, 81]. It was suggested that the stable configurations of multivacancies in silicon have "part of hexagonal ring" (PHR) configuration formed by sequentially removing atoms from a hexagonal ring (Fig. B.1(b)–(d)). However, Makhov and Lewis [66] have carried out calculations and found that the fourfold configurations of the tri-, tetra-, and penta-vacancies (Figs. B.2 and B.3) are more stable than the PHR configurations. In the fourfold configurations of tri-, tetra-, and penta-vacancies, three, two, and one interstitial atoms are introduced, respectively, into the hexavacancy and each introduced atom forms four covalent bonds (Figs. B.2 and B.3). A very recent deep-level transient spectroscopy (DLTS) measurement has found that, in the case of the trivacancy in silicon, the fourfold configuration is energetically more favorable than the PHR configuration [67], which is consistent with the results of Makhov and Lewis.

As mentioned above, the stability of silicon multivacancies has been extensively studied. Moreover, magic numbers of multivacancies of GaAs [82] and graphene [83] were also studied. However, little is known for the stability of germanium multivacancies.

In this study, we carry out the density-functional-theory calculations to study the stability of germanium vacancies. We also carry out calculations of silicon vacancies and compare the results of germanium and silicon. In the case of the tri-, tetra-, and penta-vacancies in silicon, we show that the fourfold configurations are more stable than the PHR ones. As for germanium, the results of tetra- and penta-vacancies give a similar conclusion with those in silicon. However for trivacancy, we find that the fourfold configuration is less stable by 0.1 – 0.2 eV than the PHR configuration.

B.2 Computational Details

We simulate defects by using supercells containing 216 atomic sites. The Brillouin-zone integration is carried out using a 8-points Monkhorst-Pack grid ($k_{MP} = 8$) [54]. We check the convergence for the di- and tri-vacancies by carrying out

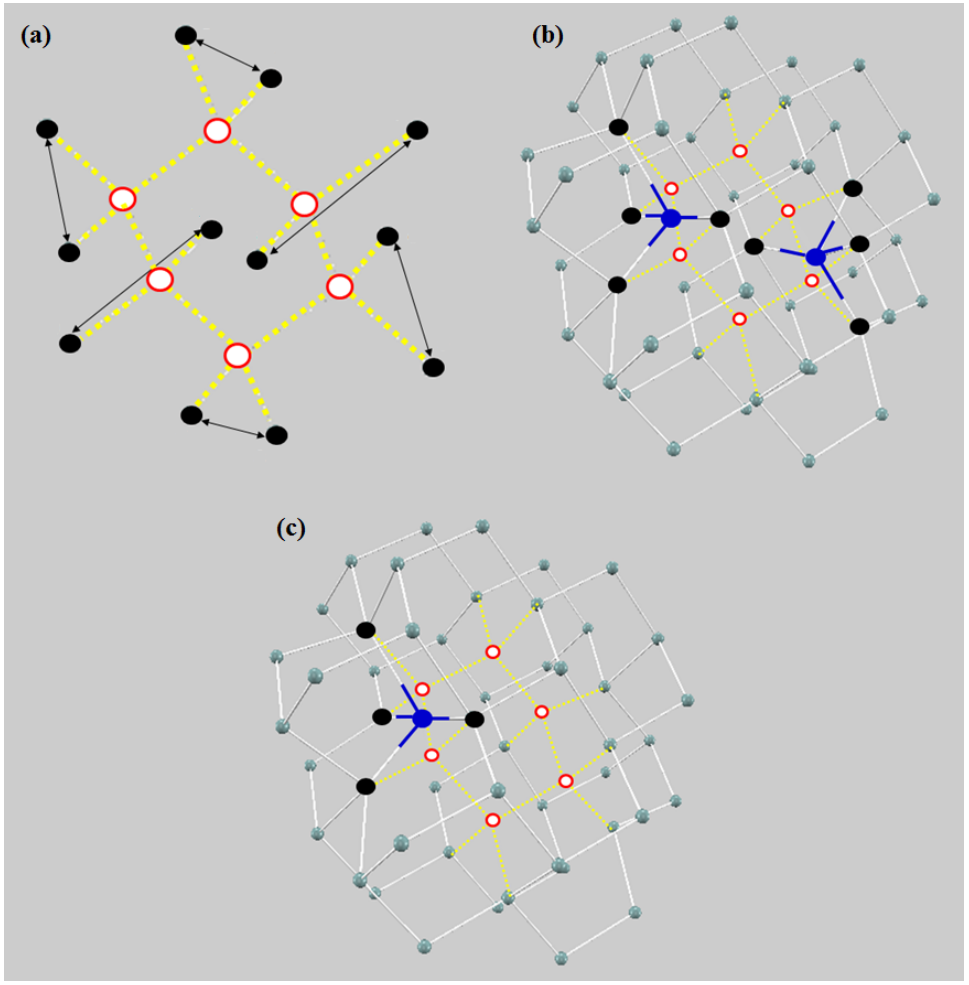

FIGURE B.2: Fourfold configurations. The hexavacancy is shown in (a). The fourfold configurations of the tetra- and penta-vacancies are shown in (b) and (c), respectively. Red open-circles represent vacancies, and blue and black closed-circles do interstitial atoms and their nearest-neighboring atoms, respectively.

calculations using 64 points and find that the formation energy differences are less than 0.1 eV. We use the 216 atomic-sites supercells since we confirmed the convergence: we check the convergence for the germanium trivacancy, and find that the formation energy difference between calculations from 216 and 512 site calculations are less than 0.1 eV.

To find the optimized geometry, we fully relax all atoms so that the atomic forces are less than 5 $\times 10^{-2}$ eV/Å. We carry out calculations of the multivacancies for the vacancy size $1 \leq N_v \leq 6$. We simulate two configurations, the PHR

and fourfold configurations, for the tri-, tetra-, and pentavacancies. The PHR configurations are formed by sequentially removing three, four, or five atoms from the hexagonal ring. The hexavacancy forming a hexagonal ring in Fig. B.1(a) has twelve nearest-neighboring atoms with twelve broken bonds. After relaxation, each two neighboring atoms pairs so that six new bonds are created (Fig. B.2(a)). Thus, there is no broken bond at all in the hexagonal-ring configuration. As for the PHR configurations, there are two broken bonds left at the ends of the vacancy chain Fig. B.1(b)–(d).

The fourfold configurations are formed by introducing three, two, or one self-interstitial atoms to the ring-hexavacancies for the tri-, tetra-, and penta-vacancies, respectively. Each self-interstitial atom makes new bonds with four neighboring-atoms while the others pair, as in the PHR configuration; thus, there is no broken bonds at all (Figs. B.2(b)–(c) and B.3). This configuration is expected to be stable due to the decrease of broken bonds [66, 77]. We next determine the symmetry of each configuration by using point group analysis, which is described in Appendix A.1.

We calculate the formation and dissociation energies for each defect system. The formation energy (E^f) is calculated as [3, 5, 74]

$$E^f = E_v - (\frac{M - N_v}{M})E_M, \tag{B.1}$$

where E_M is the total energy of the perfect supercell consisting of M sites, E_v is the total energy of the vacancy system, and N_v is the number of vacancies. We calculate two types of the dissociation energies D_1 and D_2, which are respectively given by Eqs. (B.2) [47, 78, 79] and (B.3) [44, 47, 82]:

$$D_1 = E^f_{N_v-1} + E^f_1 - E^f_{N_v}, \tag{B.2}$$

and

$$D_2 = E^f_{N_v+1} + E^f_{N_v-1} - 2E^f_{N_v}, \tag{B.3}$$

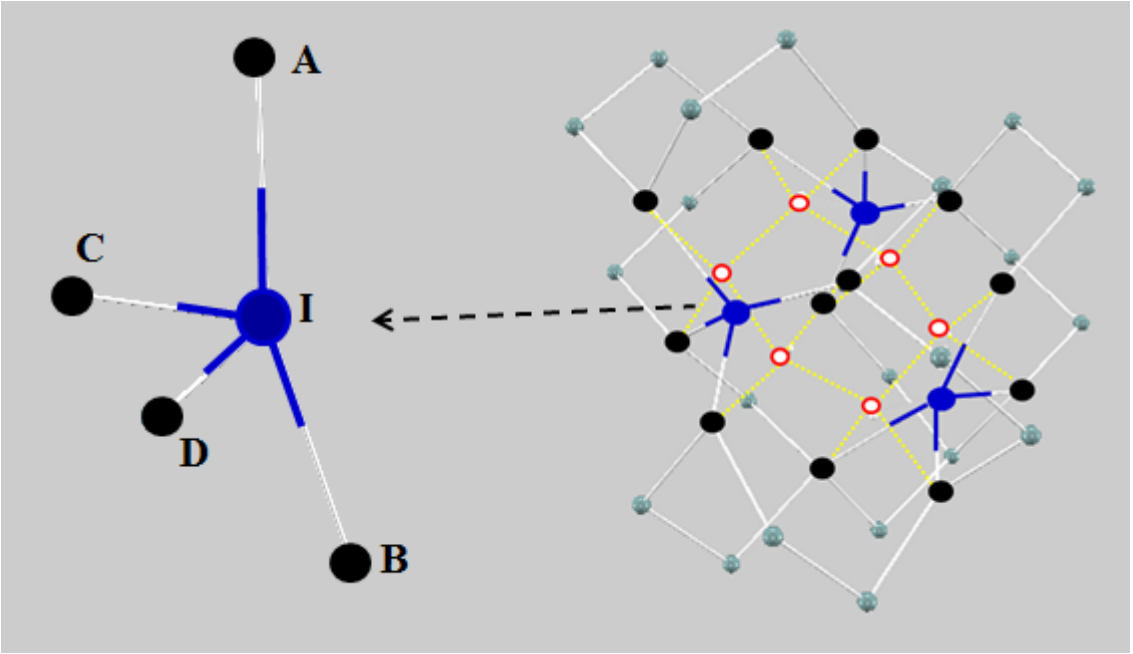

FIGURE B.3: The fourfold configuration of the trivacancy. The blue closed-circles represent the interstitial atom while the black closed-circles (A, B, C, and D) represent their four nearest-neighboring atoms.

where $E^f_{N_v}$, $E^f_{N_v-1}$, and $E^f_{N_v+1}$ are the formation energies of the supercell containing N_v, $(N_v - 1)$, and $(N_v + 1)$ vacancies, respectively, whereas E^f_1 is the formation energy for the monovacancy.

B.3 Results and Discussion

B.3.1 Monovacancy

We first calculate formation energies of the monovacancy by using Eq. (B.1). In the silicon case, the calculated formation energy is 3.52 eV, which is in good agreement with the experimental value of 3.6 ± 0.5 eV [9]. The value calculated from the 216 site cell in the present calculation is close to that calculated from the 1728 site calculation (3.46 eV) that we presented in Chapter 3. The Jahn-Teller effect [7] lowers the symmetry, and the optimized geometry has the D_{2d} symmetry. The symmetry lowering from T_d to D_{2d} is explained in Appendix A.2.

TABLE B.1: Calculated formation energies (in eV) of the PHR and fourfold configurations in germanium and silicon. N_v is the vacancy size and E^f is the formation energy.

N_v	E^f (Ge)		E^f (Si)	
	PHR	Fourfold	PHR	Fourfold
1	2.32		3.52	
2	4.10		5.25	
3	5.67	5.79	7.08	6.38
4	7.14	6.82	8.37	7.16
5	7.96	7.74	8.97	8.23
6	8.49		9.05	

In the germanium case, we find that the calculated formation energy is 2.32 eV, which is close to the experimental value of 2.35 ± 0.11 eV [84–93]. The determined symmetry is D_{2d}, which is the same as in the silicon case. However, the germanium monovacancy has lower formation energy than the silicon monovacancy. This smaller energy of germanium is expected to be due to the weak covalent bonds. Fig. B.4 shows the charge density distribution in the perfect crystal of silicon and germanium. In the silicon case, the charge density shows one maximum peak in the bond region while in the germanium case, the charge density shows double peak (Fig. B.4). These results indicate that covalent bonds in germanium are weaker than those in silicon.

The previous theoretical studies showed that the formation energies of the germanium monovacancy are 2.0 – 2.9 eV [70–72, 94]. A recent 64-site calculation based on the Heyd-Scuseria-Ernzerhof range-separated hybrid functional [95] gives the formation energy of the germanium monovacancy of 2.87 eV.

B.3.2 Divacancy

We next study the silicon divacancy. From the electron paramagnetic resonance experiment, the pairing model was proposed [96] but a DFT study supported the

TABLE B.2: Calculated bond angles of the fourfold configurations in germanium and silicon trivacancies. The atoms denoted by A, B, C, D, and I are shown in Fig. B.3.

Bond angles	Germanium	Silicon
∠AIB	163.2°	158.4°
∠CID	106.2°	108.6°
∠AIC, ∠BID	86.9°	89.6°
∠AID, ∠BIC	102.9°	103.1°

resonant-bonding (RB) model [97, 98] whose symmetry is the same as the pairing model (C_{2h}). We find that the RB configuration has lower formation energy than the pairing one but the energy difference is very small (0.01 eV). A previous large-scale DFT calculation also reported that the both configurations have close energies [97]: The 512-site cell calculation indicates that the RB configuration has slightly 0.02 eV lower formation energy than the pairing configuration.

In the germanium case, we find that the pairing configuration has very slightly lower formation energy value (within 0.002 eV) than the RB configuration. Öğüt and Chelikowsky carried out cluster calculations and also found that two configurations have similar formation energies, i.e., the RB configuration has only 0.03 eV lower formation energy than the pairing configuration [99].

We conclude that the RB and pairing configurations have close energies in both cases of silicon and germanium; thus the determination of the most stable configurations is still unclear.

B.3.3 Trivacancy

We calculate formation energies of the PHR and fourfold configurations for the trivacancy. In the fourfold configuration, three interstitial atoms are introduced in the hexavacancy (Fig. B.3). We find that the geometries of silicon and germanium trivacancies have D_3 symmetries.

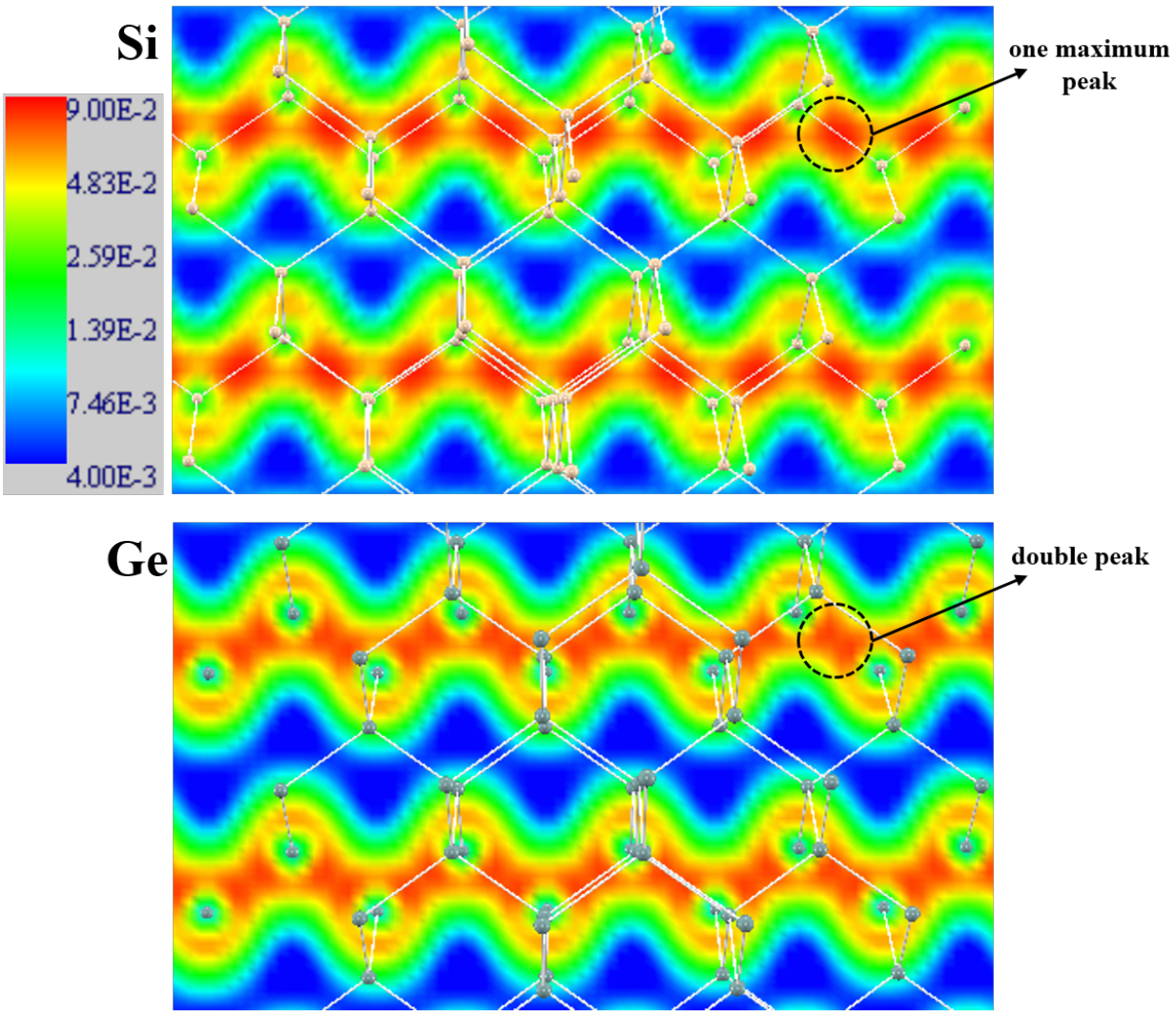

FIGURE B.4: Charge density distributions in the perfect supercell of silicon (top) and germanium (bottom). The unit in the color bar is $e/(\text{a.u.})^3$.

In the case of silicon, we find that the fourfold configuration has 0.70 eV lower formation energy than the PHR configuration (Table B.1). On the other hand, we find that the fourfold configuration has 0.12 eV higher formation energy than the PHR configuration in the case of germanium (Table B.1). Therefore, the most stable configurations of the silicon and germanium are different.

As for the germanium trivacncy, we check the convergence of the formation energy difference by carrying out two calculations. The first calculation is carried

out by using a GGA-based 216-sites calculation and we find that the fourfold configuration has 0.20 eV higher formation energy than the PHR configuration. The second calculation is carried out by using a 512-sites calculation and we find that the formation energy difference is 0.13 eV lower in the case of the PHR configuration. These results are very close to that calculated from the LDA-based 216-sites calculation (0.12 eV); thus, our calculated result well converges.

Each of the interstitial atoms introduced in the hexavacancy forms four bonds (Fig. B.3). As is shown in Table B.2, the deviations from the sp^3 ideal bond angle (109.5°) in the case of germanium are larger than those in the case of silicon. This result indicates that the four bonds in the germanium trivacancy are weaker than those of the silicon trivacancy. To confirm the weak covalent bonds, we calculate the ratio of the bond-length of the four bonds of the interstitial atom to that of the crystal. We find that the ratios in the germanium trivacancy are 1.06 – 1.13, which are larger than the corresponding values (1.04 – 1.11) in the silicon trivacancy (Table B.3). These results also indicate that the bonds in the germanium trivacancy are weak. Moreover, the charge density calculation shows that the bonding charge between the interstitial atom I and its four nearest-neighboring atoms (i.e., atom A and atom C) in the case of germanium is lower than that in the case of silicon (Fig. B.5).

B.3.4 Multivacancies

We carry out calculations of the multivacancies whose sizes are $4 \leq N_v \leq 6$. In the case of the tetra- and penta-vacancies, we carry out calculations of the PHR and fourfold configurations. In the case of silicon, the fourfold configurations have lower formation energies than the PHR configurations by 1.21 and 0.74 eV for the tetra- and penta-vacancies, respectively (Table B.1). The determined symmetries of the fourfold configurations are C_{2h} and C_2, respectively. These results are consistent with those of the previous DFT study [66].

In the case of germanium, the fourfold configurations of the tetra- and penta-vacancies have lower formation energies than the PHR configurations as in the

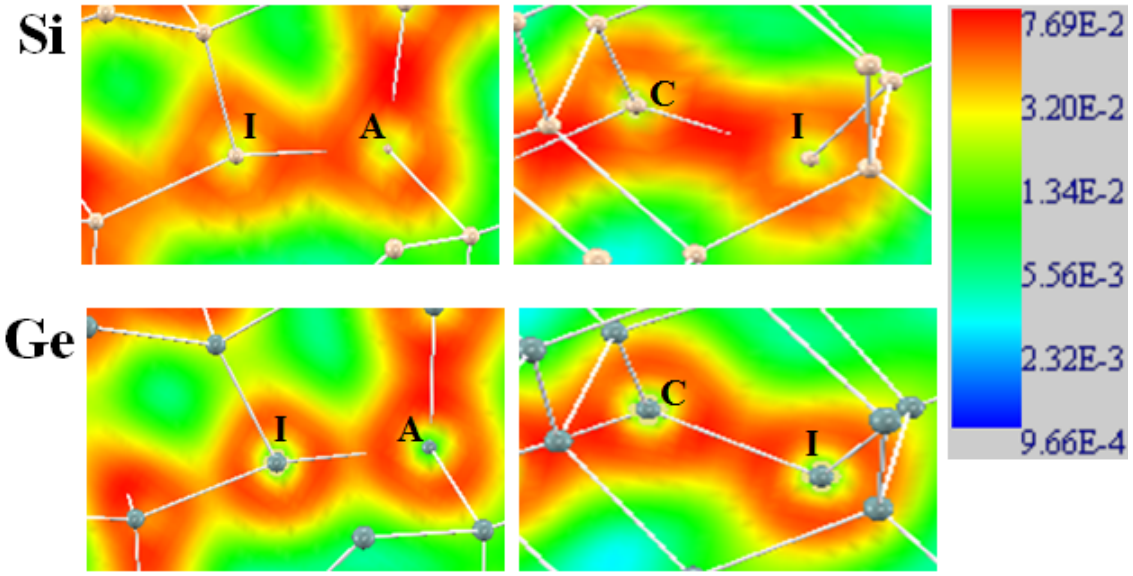

FIGURE B.5: Charge density distribution in the fourfold configuration of the silicon (top) and germanium (bottom) trivacancies. Atoms denoted by A, C, and I are shown in Fig. B.3. The unit in the color bar is $e/(\text{a.u.})^3$.

silicon case. However, the formation energy differences are 0.32 and 0.22 eV, respectively and thus the differences are smaller than the corresponding values in the case of silicon (Table B.1). These small formation-energy differences in the germanium tetra- and penta-vacancies are expected to be due to the fact that the four bonds of the interstitial atoms are weak as in the case of the trivacancy. We find the symmetries are C_{2h} and C_2 for the tetra-, and penta-vacancies, respectively, as in the silicon case.

We finally calculate the formation energies of the hexavacancies. The formation energies are 8.49 and 9.05 eV in the cases of germanium and silicon, respectively. The formation energy differences between the hexavacancies and pentavacancies are small, which are 0.53 eV in the case of germanium and 0.08 eV in the case of silicon (Table B.1); thus, the hexavacancies are expected to be stable. We find the D_{3d} symmetry in both cases of germanium and silicon hexavacancies.

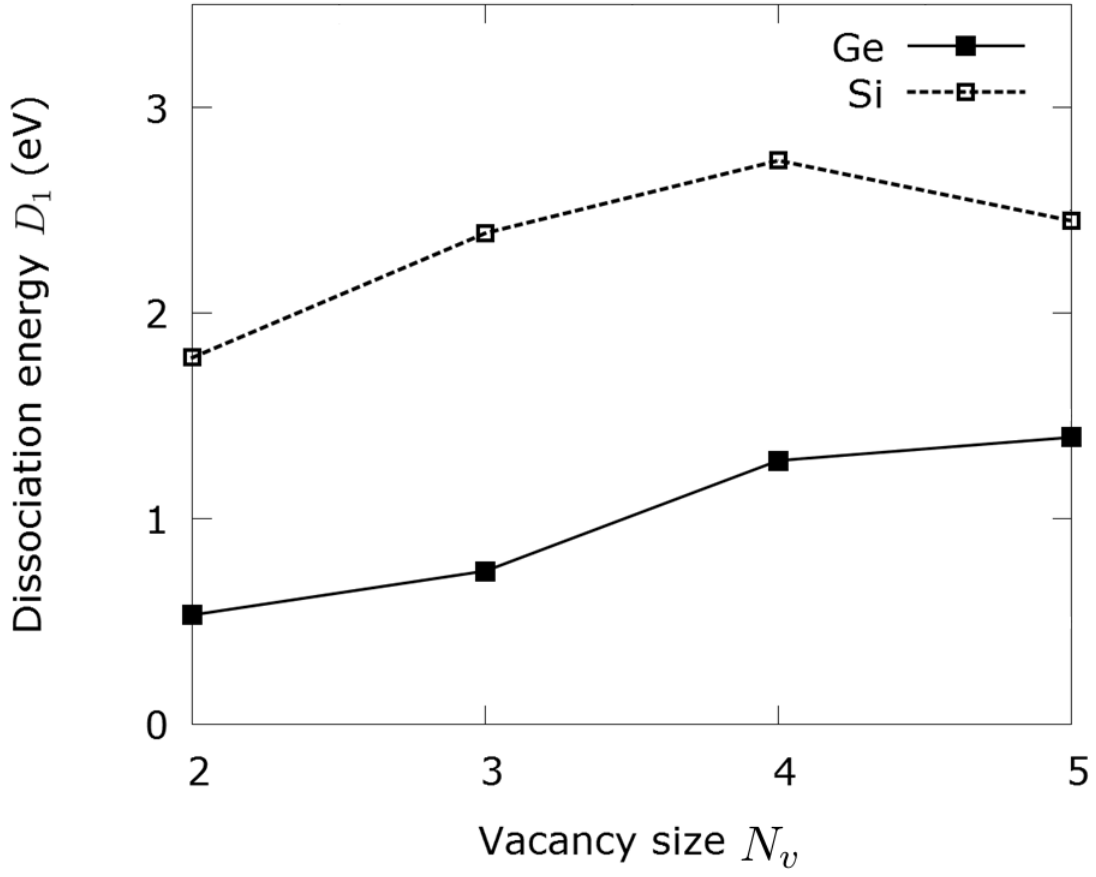

FIGURE B.6: Calculated dissociation energies (D_1) of the most stable configurations as a function of vacancy size N_v. The dashed and solid lines represent the silicon and germanium cases, respectively.

B.3.5 The dissociation energy

We here calculate dissociation energies D_1 (Eq. (B.2)) and D_2 (Eq. (B.3)) of the most stable configurations from divacancy to pentavacancy. D_1 is the binding energy for the vacancy reaction $V_{N_v} \rightarrow V_{N_v-1} + V$ whereas D_2 is the dissociation energy for the vacancy reaction $2V_{N_v} \rightarrow V_{N_v+1} + V_{N_v-1}$ [47]. The calculated dissociation energies are shown in Figs. B.6 and B.7 for D_1 and D_2, respectively.

In the silicon case, we find that the tetravacancy has the energy peak, which suggests that the tetravacancy is not easy to dissociate and is thus stable. Meanwhile,

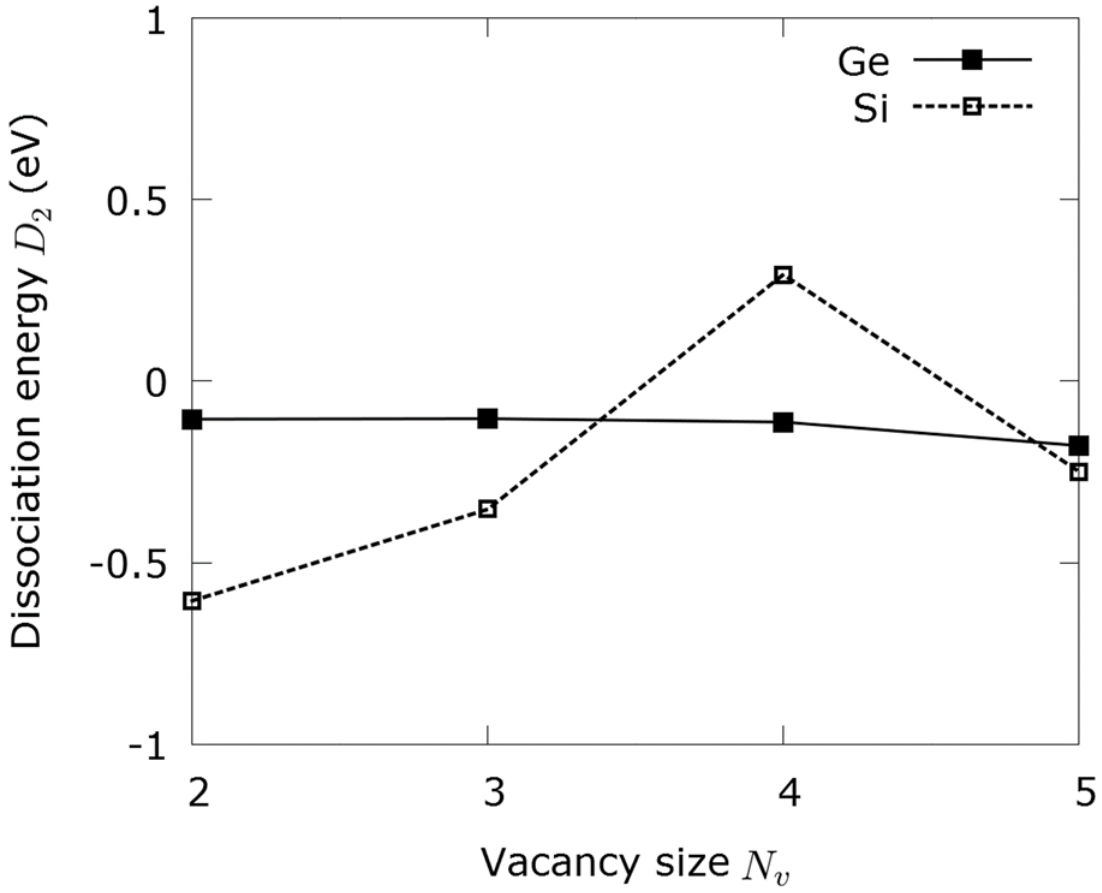

FIGURE B.7: Calculated dissociation energies (D_2) of the most stable configurations as a function of vacancy size N_v. The dashed and solid lines represent the silicon and germanium cases, respectively.

there is no peak in the case of germanium. Therefore, the germanium tetravacancy is not so stable compared with the silicon tetravacancy.

To confirm the stability of the silicon tetravacancy, we calculate the ratio of the bond-length of the four bonds of the interstitial atom to that of the crystal. We find that the ratios in the silicon tetravacancy are 1.04 – 1.08, which are smaller than the corresponding values (1.05 – 1.11) in the germanium tetravacancy. We also find that the deviations from the sp^3 ideal bond angle in the case of silicon are smaller than those in the case of germanium. These results indicate that the bonds in the silicon tetravacancy are strong and thus the silicon tetravacancy is not easy to dissociate.

TABLE B.3: Calculated bond lengths (L) of the fourfold configurations in germanium and silicon trivacancies. The atoms denoted by A, B, C, D, and I are shown in Fig. B.3. The crystal bond lengths (L_0) are 2.43 and 2.37 Å for germanium and silicon, respectively. Ratio of the fourfold bond and crystal bond lengths are also shown.

Bond	Germanium		Silicon	
	L (Å)	Ratio	L (Å)	Ratio
I-A	2.74	1.13	2.64	1.11
I-B	2.74	1.13	2.64	1.11
I-C	2.57	1.06	2.47	1.04
I-D	2.57	1.06	2.47	1.04

B.4 Conclusion

We have carried out DFT calculations of multivacancies in germanium and silicon. For the monovacancy, we found that the optimized geometry has the D_{2d} symmetry for both germanium and silicon. The formation energy is smaller in germanium than that in silicon, which is expected to be due to the fact that the covalent bonds in germanium are weaker than those in silicon. In the case of the divacancy, we found that the RB and pairing configurations have close energies in both cases of silicon and germanium. In the case of the trivacancy, the fourfold configuration is the most stable in silicon but the PHR is the most stable in germanium. This difference between silicon and germanium is expected to be due to the fact that the covalent bonds of the interstitial atoms in the fourfold configuration are weak in the case of germanium. As for the tetra- and penta-vacancies, the fourfold configurations are the most stable in both cases of silicon and germanium. However, the energy differences between the most stable fourfold configurations and metastable PHR ones are small in the case of germanium compared with the case of silicon, which is expected to originate from the fact that the covalent bonds of the interstitial atoms in the fourfold configurations are weak in germanium as in the case of the trivacancy. By calculating dissociation energies, we find that the silicon tetravacancy is not easy to dissociate and is thus stable whereas the germanium tetravacancy is not so stable compared with the silicon one.

In this study, we find prominent differences between the silicon and germanium multivacancies. Experiments of germanium multivacancies such as DLTS and electron paramagnetic resonance are expected to confirm these difference.

Bibliography

[1] M. Riordan, L. Hoddeson, and C. Herring, Rev. Mod. Phys **71**, S336 (1999).

[2] I. M. Ross, IEEE Proc., **86**, 7 (1998).

[3] F. Corsetti and A. A. Mostofi, Phys. Rev. B **84**, 035209 (2011).

[4] A. F. Wright, Phys. Rev. B **74**, 165116 (2006).

[5] M. I. J. Probert and M. C. Payne, Phys. Rev. B **67**, 075204 (2003).

[6] F. El-Mellouhi, N. Mousseau, and P. Ordejón, Phys. Rev. B **70**, 205202 (2004).

[7] For a review, see: G. D. Watkins, *Defects and Their Structure in Non-metallic Solids* (Plenum, New York, 1976) p. 203.

[8] S. Dannefaer, P. Mascher, and D. Kerr, Phys. Rev. Lett. **56**, 2195 (1986).

[9] G. Watkins and J. Corbett, Phys. Rev. **134**, A1389 (1964).

[10] Y. Shimizu, M. Uematsu, and K. M. Itoh, Phys. Rev. Lett. **98**, 095901 (2007).

[11] N. Fukata, A. Kasuya, and M. Suezawa, Physica B **308-310**, 11251128 (2001).

[12] T. Goto, H. Yamada-Kaneta, Y. Saito, Y. Nemoto, K. Sato, K. Kakimoto, and S. Nakamura, J. Phys. Soc. Jpn. **75**, 044602 (2006).

[13] M. Suezawa and Y. Yonenaga, J. Phys. Soc. Jpn. **76**, 076001 (2007).

[14] K. Uchida and A. Oshiyama, J. Phys. Soc. Jpn. **79**, 093711 (2010).

[15] J. Vanhellemont, J. Lauwaert, A. Witecka, P. Śpiewak, I. Romandic, and P. Clauws, Physica B **404**, 4529 (2009).

[16] D. Kuzum, T. Krishnamohan, A. Nainani, Y. Sun, P. A. Pianetta, H. S. P. Wong, and K. C. Saraswat, IEDM Dig. of Tech. Papers, 19.1.1 (2009).

[17] H. Wu, N. Conrad, W. Luo, and P. D. Ye, IEDM Dig. of Tech. Papers, 9.3.1 (2014).

[18] S. M. Sze, *Physics of Semiconductor Devices* (John Wiley and Sons, New York, 1981).

[19] For a review, see: S. Wolf, R. Tauber, *Silicon Processing for the VLSI Era* (Lattice Press, California, 1986).

[20] Mitard et al., IEDM Dig. of Tech. Papers, 873 (2008).

[21] Kuzum et al., IEDM Dig. of Tech. Papers, 723 (2007).

[22] Shang et al., IEEE Electron Dev. Lett. **25**, 135 (2004).

[23] Whang et al., IEDM Dig. of Tech. Papers, 307 (2004).

[24] D. S. Sholl and J. A. Steckel, *Density Functional Theory: A Practical Introduction* (John Wiley and Sons, New Jersey, 2009).

[25] http://www.ciss.iis.u-tokyo.ac.jp/english/dl/.

[26] D. R. Hartree, Proc. Cambridge Phil. Soc. **24:89**, 426 (1928).

[27] P. Hohenberg and W. Kohn, Phys. Rev. B **136**, 864 (1964).

[28] W. Kohn and L. J. Sham, Phys. Rev. A **140**, 1133 (1965).

[29] A. D. Becke, Phys. Rev. A **38**, 3098 (1988).

[30] J. P. Perdew, J. A. Chevary, S. H. Vosko, K. A. Jackson, M. R. Pederson, and C. Fiolhais, Phys. Rev. B **46**, 6671 (1992).

[31] J. P. Perdew and Y. Wang, Phys. Rev. B **46**, 6671 (1992).

[32] J. P. Perdew, K. Burke, and M. Ernzerhof, Phys. Rev. Lett. **77**, 3865 (1996).

[33] J. Kohanoff, *Electronic Structure Calculation for Solids and Molecules: Theory and Computational Methods* (Cambridge University Press, United Kingdom, 2006) p. 85.

[34] P. S. Svendsen and U. von Barth, Phys. Rev. B **54**, 17402 (1996).

[35] J. P. Perdew and K. Burke, Int. J. Quant. Chem. **57**, 309 (1996).

[36] D. R. Hamann, M. SchlNuter, and C. Chiang, Phys. Rev. Lett. **43**, 1494 (1979).

[37] D. Vanderbilt, Phys. Rev. B **41**, 7892 (1990).

[38] F. Birch, Phys. Rev. **71**, 809 (1947).

[39] K. K. Zhuravlev, Physica B **394**, 1 (2007).

[40] K. Levenberg, Quart. Appl. Math. **2**, 164 (1944).

[41] D. W. Marquardt, SIAM J. Appl. Math. **11**, 431 (1963).

[42] H. P. Singh, Acta Cryst. **A24**, 469 (1968).

[43] P. Becker, P. Scyfried, and H. Siegert, Z. Phys. B **48**, 17 (1982).

[44] A. Oshiyama, M. Saito, and O. Sugino, Appl. Surf. Sci. **85**, 239 (1995).

[45] A. Antonelli, E. Kaxiras, and D. J. Chadi, Phys. Rev. Lett. **81**, 2088 (1998).

[46] O. K. Al-Mushadani and R. J. Needs, Phys. Rev. B **68**, 235205-3 (2003).

[47] M. Saito, A. Oshiyama, and S. Tanigawa, Phys. Rev. B **44**, 10 601 (1991).

[48] G. D. Watkins and J. R. Troxell, Phys. Rev. Lett. **44**, 593 (1980).

[49] G. Baraff, E. Kane, and M. Schlutter, Phys. Rev. Lett. **43**, 956 (1979).

[50] V. V. Voronkov, J. Cryst. Growth **59**, 625 (1982).

[51] P. M. Fahey, P. B. Griffin, and J. D. Plummer, Rev. Mod. Phys. **61**, 289 (1989).

[52] M. J. Puska, S. Pöykkö, M. Pesola, and E. M. Nieminen, Phys. Rev. B **58**, 1318 (1998).

[53] P. Śpiewak and K. J. Kurzydłowski, Phys. Rev. B **88**, 195204 (2013).

[54] H. J. Monkhorst and J. D. Pack, Phys. Rev. B **13**, 5188 (1976).

[55] C. W. M. Castleton, A. Höglund, and S. Mirbt, Phys. Rev. B **73**, 035215 (2006).

[56] M. Leslie and M. J. Gillan, J. Phys. C **18**, 973 (1985).

[57] G. Makov and M. C. Payne, Phys. Rev. B **51**, 4014 (1995).

[58] M. Sanati and S. K. Estreicher, Solid State Commun. **128**, 181 (2003).

[59] J. J. Burton, Phys. Rev. B **5**, 2948 (1972).

[60] V. V. Voronkov and R. Falster, J. Appl. Phys. **87**, 4126 (2000).

[61] E. Dornberger, D. Graf, M. Suhren, U. Lambert, P. Wagner, F. Dupret, and W. von Ammon, J. Cryst. Growth **180**, 343 (1997).

[62] M. Lannoo and G. Allan, Phys. Rev. B **25**, 4089 (1982).

[63] M. Lannoo and G. Allan, Phys. Rev. B **33**, 8789 (1985).

[64] J. R. Leite, E. C. F. da Silva, and A. Dal Pino, Mater. Sci. Forum **38-41**, 263 (1989).

[65] D. V. Makhov and L. J. Lewis, Phys. Rev. Lett. **92**, 255504 (2004).

[66] V. P. Markevich, A. R. Peaker, S. B. Lastovskii, L. I. Murin, J. Coutinho, V. J. B. Torres, P. R. Briddon, L. Dobaczewski, E. V. Monakhov, and B. G. Svensson, Phys. Rev. B **80**, 235207 (2009).

[67] H. A. Jahn and E. Teller, Proc. Roy. Soc. A **161**, 220 (1927).

[68] Q. Pang, Y Zhang, J-M Zhang, V. Ji, and K-W Xu, Mater. Chem. Phys. **130**, 140 (2011).

[69] P. Śpiewak, J. Vanhellemont, K. Sueoka, K. J. Kurzydłowski, and I. Romandic, J. Appl. Phys. **103**, 086103 (2008).

[70] H. M. Pinto, J. Coutinho, V. J. B. Torres, S. Öberg, and P. R. Briddon, Materials Science in Semiconductor Processing **9**, 498 (2006).

[71] E. Kamiyama, K. Sueoka, and J. Vanhellemont, ECS J. Solid State Sci. Technol. **2 (3)**, P104 (2013).

[72] J. Coutinho, V. P. Markevich, A. R. Peaker, S. B. Lastovskii, L. I. Murin, B. Hamilton, B. J. Svensson, M. J. Rayson, and P. R. Briddon, Phys. Rev. B **86**, 174101 (2012).

[73] C. Janke, R. Jones, S. Öberg, and P. R. Briddon, Phys. Rev. B **75**, 195208 (2007).

[74] M. C. Petersen and A. N. Larsen, Phys. Rev. B **82**, 075203 (2010).

[75] J. Slotte, S. Kilpeläinen, F. Tuomisto, J. Räisänen, and A. N. Larsen, Phys. Rev. B **83**, 235212 (2011).

[76] D. J. Chadi and K. J. Chang, Phys. Rev. B **38**, 1523 (1988).

[77] T. E. M. Staab, A. Sieck, M. Haugk, M. J. Puska, T. Frauenheim, and H. S. Leipner, Phys. Rev. B **65**, 115210 (2002).

[78] S. Lee and G. S. Hwang, Phys. Rev. B **78**, 125310 (2008).

[79] J. L. Hastings and S. K. Estreicher, Phys. Rev. B **56**, 10215 (1997).

[80] S. K. Estreicher, Phys. Status Solidi (b) **217**, 513 (2000).

[81] T. E. M. Staab, M. Haugk, A. Sieck, Th. Frauenheim, and H. S. Leipner, Physica B **273-274**, 501 (1999).

[82] M. Saito, K. Yamashita, and T. Oda, Jpn. J. Appl. Phys. **46**, L1185 (2007).

[83] J. Vanhellemont, P. Śpiewak, and K. Sueoka, J. Appl. Phys. **101**, 036103 (2007).

[84] S. Mayburg, Phys. Rev. **95**, 38 (1954).

[85] R. A. Logan, Phys. Rev. **101**, 1455 (1956).

[86] A. G. Tweet, Phys. Rev. **106**, 221 (1957).

[87] A. G. Tweet, J. Appl. Phys. **30**, 2002 (1959).

[88] A. Hiraki, J. Phys. Soc. Jpn. **21**, 34 (1952).

[89] A. D. Belyaev, L. I. Datsenko, and S. S. Malogolovets, Ukr. Fiz. Zh. (Russ. Ed.) **12**, 655 (1967).

[90] S. Samuelsson, Ark. Fys. **35**, 321 (1967).

[91] L. F. Konorova, Sov. Phys. Solid State **10**, 2233 (1969).

[92] A. Giese, N. A. Stolwijk, and H. Bracht, Appl. Phys. Lett. **77**, 642 (2000).

[93] P. Śpiewak, K. Sueoka, J. Vanhellemont, K. J. Kurzydłowski, K. Młynarczyk, P. Wabiński, and I. Romandic, Physica B **401-402**, 205 (2007).

[94] P. Śpiewak, J. Vanhellemont, and K. J. Kurzydłowski, J. Appl. Phys. **110**, 063534 (2011).

[95] G. Watkins and J. Corbett, Phys. Rev. **138**, A543 (1965).

[96] J. Iwata, K. Shiraishi, and A. Oshiyama, Phys. Rev. B **77**, 115208 (2008).

[97] H. Seong and L. J. Lewis, Phys. Rev. B **53**, 9791 (1996).

[98] S. Öğüt and J. R. Chelikowsky, Phys. Rev. B **64**, 245206 (2001).